Fluorinated Nanoparticles: A Novel Technology Platform for Multimodal Biomedical Imaging Applications

BY

Mark Michael Bailey

Submitted to the graduate degree program in Bioengineering and the Graduate Faculty of the University of Kansas in partial fulfillment of the requirements for the degree of Doctor of Philosophy.

_____
Cory J. Berkland, Committee Chairperson

Committee Members: _____
Michael S. Detamore

_____
Sara Wilson

_____
Xinmai Yang

_____
Teruna Siahaan

Date Defended: _____

The Dissertation Committee of Mark Michael Bailey
certifies that this is the approved version of the following dissertation:

Fluorinated Nanoparticles: A Novel Technology Platform for Multimodal Biomedical Imaging Applications

Committee:

_____
Cory J. Berkland, Committee Chairperson

Committee Members: _____
Michael S. Detamore

_____
Sara Wilson

_____
Xinmai Yang

_____
Teruna Siahaan

To Lauren,
Without whom this would be impossible.

Acknowledgements

First, I would like to express my deepest appreciation to my mentor and advisor, Cory Berkand, for all of his support and his enduring encouragement. His commitment to the success of his students is unparalleled. Without his vision, this project would never have been possible. Second, I would like to thank Greg Gillen at NIST, who was gracious enough to provide a collaborative atmosphere in which I could pursue a large portion of my research project while learning how a government lab operates. I am grateful to him for his genuine interest in my work and for his kindness. I would also like to thank all of my colleagues and collaborators at The University of Kansas for all of their help and support: Nashwa El-Gendy, Chuda Chittasupho, Elodie Dempah, Supang Khondee, Amir Fakhari, Joshua Sestak, Abdul Baoum, Sheng-Xue Xie, Huili Guan, Kristin Aillon, Qun Wang, Carl Plumley, and Zahra Mohammadi. I would also like to thank my collaborators at NIST, including Christine Mahoney, Jeff Davis, Steven Kline, Matthew Becker (now at The University of Akron), John Elliott, Albert Fahey, Jessica Staymates, Matthew Staymates and Michael Anderson for all of their help and support and for their genuine excitement about science.

In addition to my current mentors and collaborators, I would like to express my earnest gratitude to my past mentors and teachers who have

inspired me to pursue a career in science: Michael Detamore, Jack Patzer, Joann Burak, Craig Long, Lorraine Soraparu, Ellen Gallagher, and Dennis Graham. Their mentorship, encouragement, and faith have guided me to where I am today.

I would also like to express my deepest appreciation to Madison and Lila Self, whose generous contribution to the University of Kansas in the form of the Madison and Lila Self Graduate Fellowship has enabled many students, including myself, to gain an education beyond education. My sincere thanks go to the current and former staff of the Self Graduate Fellowship: Howard Mossberg, Cathy Dwigans, Sharon Graham, Patty Dannenberg, and Jim Morrison. Their commitment to the ideals of the Fellowship and to the success of the students has made it into the outstanding program that it is today.

I would also like to thank the present and past members of my dissertation committee: Michael Detamore, Sara Wilson, Teruna Siahaan, Xinmai Yang, and Laird Forrest; for their commitment to my dissertation project and for pushing me toward excellence.

Last, but certainly not least, I would like to thank my family and friends who have supported me throughout my education.

Mark M. Bailey

July 2010

Table of Contents

Chapter 1

Bioimaging with Fluorinated Contrast Agents

1.1 Fluorinated Compounds in Medicine

Fluorinated polymers and emulsions are earning a place as tools for a variety of biomedical applications, including oxygen carriers ("artificial blood"), contrast agents for imaging, and drug delivery vehicles.[1, 2] Additionally, fluorination of drugs is a common means to impart metabolic stability and enhance tissue permeability, for example through the blood brain barrier.[3] Over the years, research in fluorinated drugs and biomaterials has resulted in a variety of novel fluorinated compounds and emulsions.

Fluorinated compounds are of great interest to the biomedical community due to their multiple unique properties. Introducing fluorine into a molecule generates novel behavior due to the high ionization potential, high electronegativity (4.0 on the Pauling scale), and low polarizability of this atom.[4] Fluorine has a van der Waals radius of 1.47 Å, making it larger than hydrogen, which has a van der Waals radius of 1.20 Å.[5] Fluorine is as space filling as oxygen, yet is much less polarizable. Perfluorocarbons have a larger cross section than their hydrocarbon counterparts due to the larger size of fluorine, and have a helical structure rather than the planar, zig-zag structure common to hydrocarbons. Additionally, the conformational freedom of perfluorocarbons is reduced due to their greater gauche/trans interchange energy (4.6 $kJmol^{-1}$) than

hydrocarbons (2.0 $kJmol^{-1}$). As a consequence, the occurrence of gauche defects is reduced, thereby facilitating stacking and ordering of fluorocarbon chains at equilibrium conditions.[1, 6, 7]

One of the most fascinating properties of fluorinated compounds is their simultaneous hydrophobicity and lipophobicity. This promotes self-aggregation, phase separation and the exclusion of non-fluorinated materials from fluorinated emulsions.[1] These properties are often exploited in drug delivery applications, where the increased lipophobicity imparted by fluorine facilitates permeation of the blood brain barrier (BBB), especially in neuroleptics and selective serotonin reuptake inhibitors (SSRI) such as fluoxetine, citalopram, and paroxetine.[3]

Perfluorocarbons are some of the most thermally stable compounds known and are highly chemically inert due to the strength of the C-F bond, which is the strongest single bond known in organic chemistry. The electronegativity of fluorine reinforces the carbon backbone of perfluorocarbons, and creates a compact electron shield that protects the carbon-carbon bonds from approaching reagents.[1] Because of this stability, perfluorocarbons typically do not detrimentally interact with cells and tissues. Studies have shown that fluorinated surfactants consistently exhibit lower hemolytic activity than their hydrogenated

counterparts, although their pharmacokinetics and potential chronic toxicity still need to be evaluated.[8, 9]

In contrast to their strong intramolecular bonds, perfluorocarbons exhibit very low intermolecular cohesion. The low polarizability of fluorine results in lower van der Waals interactions between molecules, thus reducing their attractiveness to one another. Thus, liquid perfluorocarbons behave nearly like an ideal gas.[1] Fluorinated liquids have high vapor pressures compared to their corresponding hydrocarbons, making them a strong candidate for use in gas-filled microbubbles, which have been demonstrated as ultrasound contrast agents.[1, 2] Additionally, their weak intermolecular cohesion gives perfluorocarbons extremely high oxygen and carbon dioxide dissolving capacities that are on the order of 50 vol % and 200 vol %, respectively.[1] This property makes them suitable for use in “artificial blood” applications, which could help mitigate allogeneic blood shortages and, in the future, may make them useful as a preservative to prevent organ hypoxia prior to transplantation.[1, 2]

In addition to the novel chemical properties it endows to fluorocarbons, fluorine also has interesting nuclear properties that are biologically relevant. Fluorine is a monoisotopic element, meaning that it has only one stable isotope found in nature, fluorine-19. The high abundance of fluorine-19 compared to other fluorine isotopes, combined

with the fact that fluorine-19 has a net magnetic moment (due to its odd number of neutrons and protons), make fluorine-19 ideally suited for use as a nuclear magnetic resonance imaging (MRI) contrast agent.[10, 11]

A synthetic isotope of fluorine commonly used in medical imaging is fluorine-18. This isotope is used in positron emission tomography (PET) imaging and has a half-life of approximately 110 minutes and decays via positron emission (β^+) to oxygen-18. The relatively long half-life of fluorine-18 and its decay into a non-toxic daughter nucleus make it ideal for PET imaging. [10, 12]

Secondary ion mass spectrometry (SIMS) imaging is an emerging *in vitro* imaging technique that could utilize fluorinated contrast agents. SIMS is a mass spectrometry technique that can be used to generate a mass image of a surface.[13] Recently it has been gaining interest as a bioimaging technique looking at cells and tissue samples for diagnostic applications.[14, 15] Fluorinated contrast agents would be useful in SIMS imaging because of fluorine's anomalously high ion yield with this technique, whereby it can be easily detected.[16] Combined with fluorine's biological rarity, this suggests that fluorinated contrast agents could be designed to target specific cell markers with fluorine acting as a SIMS "chromophore." A detailed description of SIMS imaging can be found in Appendix C.

1.2 Positron Emission Tomography (PET)

Basics of Positron Emission Tomography: Positron Emission Tomography (PET) is a gamma imaging technique that utilizes positron-emitting radionuclides as a gamma ray source. As the radionuclide decays, a positron (β^+) is expelled from the nucleus and travels a short distance in the surrounding tissue before it encounters an electron, at which time both particles annihilate each other.[10, 17] The distance traveled by the positron is known as the positron range, and is typically around 1 mm.[17] Each annihilation event produces two 511 keV gamma photons that travel in opposite directions. The energies of the gamma photons correspond to the rest masses of the electron and positron, which are completely converted to energy.[17] The gamma rays are detected by an array of detectors surrounding the patient, which are electronically linked such that two detection events unambiguously occurring within a certain time frame are determined to be coincident and hence originated from the same annihilation event. These coincidence events are then reconstructed to give spatial information on the distribution of the radionuclide throughout the body.[10, 17]

In a typical PET imaging procedure, a gamma emitting contrast agent is intravenously injected and allowed to reach a steady state

concentration in the tissues of interest. Typical contrast agents include gallium-68, iodine-124, oxygen-15, and fluorine-18.[10, 17, 18] By far the most commonly used contrast agent in PET imaging is fluorine-18 due to its long half-life (~110 min). Fluorine-18 is delivered as a radiopharmaceutical; combined with glucose to form ^{18}F-fluorodeoxyglucose, shown in Figure 1.1.

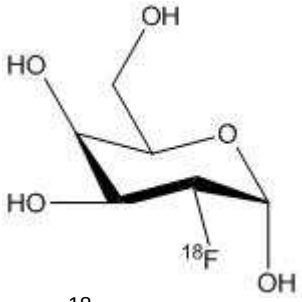

Figure 1.1: ^{18}F-Fluorodeoxyglucose

^{18}F-Fluorodeoxyglucose (FDG) accumulates rapidly in cells that utilize large quantities of glucose, such as neurons, myocytes, and cancerous cells. Being an analog of D-glucose, FDG is phosphorylated by hexokinase to ^{18}F-FDG-6-phosphate after cellular uptake, preventing it from leaving the cell.[19] The 2' hydroxyl group in glucose is necessary for continued glycolysis after the first phosphorylation step, but has been replaced by ^{18}F in FDG. Thus, FDG cannot be completely metabolized until radioactive decay occurs, at which point ^{18}F decays by positron emission into the stable isotope ^{18}O, which is subsequently protonated to a hydroxyl to allow for normal metabolism of the resultant D-glucose-6-

phosphate. As a result, the physiological distribution of FDG is a good measure of cellular glucose metabolism. For this reason, it is commonly used for tumor imaging to reveal regions of metabolically active tissue that could indicate cancer.[19]

^{18}F Radiopharmaceutical Production: ^{18}F-Fluorodeoxyglucose is synthesized using $^{18}F^-$, which is produced in a dedicated medical cyclotron using the $^{18}O(p,n)^{18}F$ nuclear reaction.[18] In this reaction, protons bombard ^{18}O enriched water to produce $^{18}F^-$ anions via the following reaction:

$$^{18}_{8}O + p^+ \rightarrow {}^{18}_{9}F^- + n^o$$

In this reaction, the ^{18}O nucleus accepts a proton, increasing its atomic number by one to fluorine. The mass number remains the same with the ejection of a neutron. After the $^{18}F^-$ ions are produced, they are collected in an ion exchange resin prior to synthesis of ^{18}F-FDG.[18] The FDG radiopharmaceutical is then produced via a nucleophilic substitution reaction between a cryptand-reinforced fluoride anion and a triflated and protected glucose derivative in acetonitrile, according to Figure 1.2.

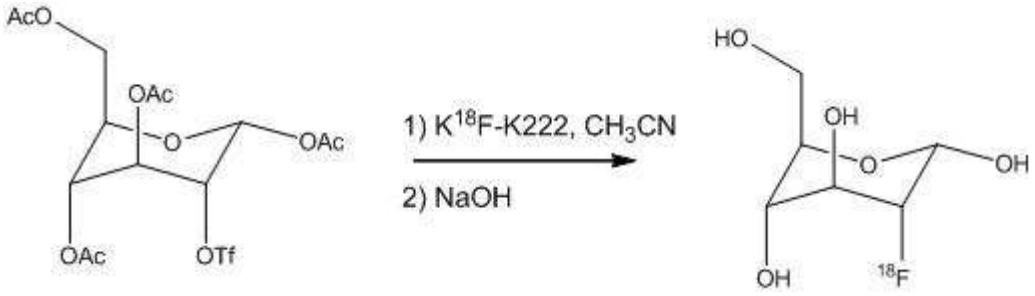

Figure 1.2: ^{18}F-fluorodeoxyglucose synthesis

In this reaction, the hydroxyl groups of the glucose molecule are protected by acetate groups, and the 2' hydroxyl group is activated for nucleophilic attack by the triflate (OTf) functional group. The potassium fluoride-K222 reagent is the ^{18}F fluoride salt, in this example bound to Kryptofix-222 (K222) as the cryptand.[18] After deprotection of the hydroxyl groups with NaOH, the resulting ^{18}F-fluorodeoxyglucose is ready for patient administration.

A new technique to incorporate fluorine-18 into a nanoparticle carrier for PET imaging has been reported by Matson and Grubbs.[12] In this technique, amphiphilic block copolymers created using ring opening metathesis polymerization (ROMP) were assembled into micelles in aqueous solution and crosslinked via a photochemical reaction, after which they were radiofluorinated. Polyethylene glycol (PEG) was used as the hydrophilic component of the copolymer due to its non-immunogenic nature, and mesylate leaving groups were added to the PEG for eventual displacement by the fluorine-18 functionality. A monomer containing a

cinnamoyl group was selected as the hydrophobic monomer to facilitate photocrosslinking. Fluorine-18 was then conjugated to the end of the hydrophilic block to replace the mesylate leaving group. This technique produced particles between 47 nm and 142 nm that might be suitable for passive targeting of tumors.[12] A technique like this may provide more selective targeting of tumors than ^{18}F-FDG, which will accumulate in any tissue with high metabolic activity.

In a study by Devaraj et al., a nanoparticle contrast agent for concurrent PET and MRI was developed using fluorine-18 as the positron source.[20] The particles contained an iron oxide core surrounded by crosslinked dextran. A PEG group containing ^{18}F was then conjugated to the surface using “click” chemistry. The authors report that PET imaging with the resultant particles showed a very high signal to noise ratio. The MRI/PET combined images suggested that the particles accumulated in the spleen, liver, and other lymphatic organs.[20] Including the iron oxide as an MRI contrast medium enables one to gather spatial information, thus providing an anatomical context for the PET data. The ability to combine multiple contrast media is one of the benefits of using nanoparticle-based imaging agents instead of traditional small molecule contrast agents.

1.3 Ultrasound Imaging

Basics of Ultrasound Imaging: Diagnostic sonography, more commonly known as ultrasound imaging, is a medical imaging technique that uses high frequency sound to measure and visualize subcutaneous features of the body, such as tendons, muscle tissue, and internal organs.[10, 21, 22] Obstetric sonography is commonly used to determine the proper growth and development of a fetus during pregnancy. The term ultrasound refers to sound waves with a frequency greater than 20 kHz, which is beyond the auditory threshold of humans.[10]

Diagnostic sonography works by focusing ultrasound waves at the tissue of interest through a sonic transducer, which is made of a piezoelectric material. The ultrasound beam is focused to a particular depth by controlling the geometry of the transducer, or by electronically controlling the timing between actuations of separate transducer elements.[10] As the ultrasound beam intercepts the boundary between two materials (e.g. transducer and skin, tissue and air, tissue and bone, etc.), a fraction of the sound is reflected as an echo and a fraction is transmitted through the boundary. This proportion depends on the relative acoustic impedances of the two materials, which is the product of the material density and the velocity of sound in the material.[10] If the incident angle of ultrasound is 90° to the interface, the reflected fraction of sound energy is given by the following equation:

$$R = \frac{(Z_1 - Z_2)^2}{(Z_1 + Z_2)^2}$$

Where Z_n are the acoustic impedances of the two materials.[10] As the difference between acoustic impedances increases, the intensity of the reflected sound increases, and the contrast of that region increases.

Contrast-enhanced ultrasound is a technique that uses ultrasound contrast medium to enhance the echogenicity of the region of interest by introducing acoustic impedance that is significantly different from typical anatomical structures. Commercially available contrast media are composed of gas-filled microbubbles that are intravenously injected prior to imaging. The compressible gas in the microbubbles oscillates when insonified, producing an acoustic impedance that is distinctly different from that of the surrounding tissue.[1, 2, 21, 22] This allows the clinician to distinguish blood from the surrounding tissues, and is often used for reperfusion imaging and tumor imaging.[10]

Fluorinated Contrast Agents: Perfluorocarbons are often used as the gas phase of ultrasound contrast microbubbles because of their ability to stabilize gaseous microbubbles in an aqueous suspension.[1, 2, 21, 22]

Microbubbles that contain air collapse under the combined arterial and Laplace pressure and begin to rapidly dissolve in the blood.[1, 2] Conversely, a microbubble composed solely of a perfluorocarbon gas will expand in circulation because of gases dissolved in the blood diffusing into the perfluorocarbon phase. For this reason, it is necessary to stabilize droplets to prevent changes in size.[1, 2]

A clinical microbubble contrast agent currently available was developed by Alliance Pharmaceutical Corporation. Imagent® is formulated as a heat-sterilized, spray-dried powder stored under a nitrogen-diluted perfluorohexane atmosphere. The powder contains dimyristoylphosphatidylcholine, hydroxyethylstarch, poloxamer, and salts to maintain tonicity. After suspension in water, the mixture forms a phospholipid monolayer that traps the gas mixture in the headspace, forming echogenic microbubbles.[1, 23]

For some applications, it is desirable to develop microbubbles that will target specific tissue types for imaging. In one study by Weller et al., perfluorobutane-filled microbubbles were synthesized and conjugated with antibodies to target intercellular adhesion molecule-1 (ICAM-1), which is upregulated in the endothelium at sites of inflammation to facilitate migration of circulating leukocytes into the surrounding tissue.[24] Human coronary endothelial cells were grown to confluence, stimulated to

inflammation with interleukin-1β (IL-1β) and incubated with anti-ICAM-1 antibody conjugated microbubbles. The authors reported that targeted microbubbles detected the presence and severity of endothelial dysfunction ranging from normal to maximal inflammation.[24]

In another study, microcapsules were synthesized that contain liquid perfluorocarbons as an echogenic medium, which are considerably easier to work with than gaseous perfluorocarbons.[22] In this method, poly(lactic-co-glycolic) acid (PLGA) and liquid perfluorocarbon (perfluorooctyl bromide, pefluoropentane, perfluorohexane, perfluorooctane, or perfluorodecalin) were dissolved in dichloromethane. The organic solution was then emulsified into an aqueous solution containing sodium cholate as a surfactant and the organic solvent was evaporated.[22] Because of the concurrent hydrophobicity and lipophobicity of the perfluorocarbon liquid, the emulsion droplets formed a core-shell structure with the perfluorocarbon in the center of a PLGA shell stabilized by sodium cholate. The authors were able to obtain both microbubbles and nanobubbles with this method, depending on the amount of shear applied during the emulsification.[22] In a later study, the authors synthesized perfluorooctyl bromide-containing bubbles with mean diameters ranging between 70 nm and 25 μm. The authors found that *in*

vivo nanocapsule injections produced significant ultrasound enhancement of the blood during hepatic imaging.[21]

1.4 Magnetic Resonance Imaging (MRI)

Basics of Magnetic Resonance Imaging: Magnetic resonance imaging (MRI) is a non-invasive, *in vivo* imaging technique that utilizes magnetic fields to visualize soft tissues within the body. MRI provides greater resolution of soft tissues than CT and x-ray imaging, which makes it especially useful in neurological, cardiovascular, and oncological imaging. MRI is presumed safer than PET, CT and x-ray imaging because it does not utilize ionizing radiation.[10]

MRI uses strong magnetic fields (typically between 0.15 T and 3 T) to align the nuclear magnetic moments of magnetically active nuclei in the body with an external magnetic field.[10] Typical anatomical imaging focuses on ^{1}H hydrogen nuclei, which is the most abundant element in the body. When in the presence of an external magnetic field, the magnetic moment of the hydrogen nuclei precess around the external magnetic field at a frequency (known as the Larmor frequency) that is dependent on the gyromagnetic ratio of the nucleus and the strength of the external magnetic field, given by:

$$\nu = \gamma \cdot B$$

where ν is the Larmor frequency (MHz), γ is the gyromagnetic ratio (MHz/T), and B is the magnitude of the external magnetic field.[10, 25]

Precession of nuclear magnetic moments is easily described in terms of classical physics, but is more accurately described as a quantum mechanical process. The individual nuclear magnetic moments will align themselves with the external magnetic field in two degenerate quantum states: either parallel or anti-parallel, because of the two possible spin states of the nucleus (±½). The ratio of nuclei in each state is roughly 1:1, however the anti-parallel state is slightly more energetic than the parallel state. For this reason, there are generally more nuclei in the parallel state than the anti-parallel state, hence there is a net magnetic moment generated within the tissue that is parallel to the external magnetic field. This vector is denoted as M_o, and precesses at the same frequency as the nuclear magnetic moments. The energy difference between the two degenerate states is proportional to the external magnetic field strength; hence the magnitude of M_o increases as B increases.[10, 25]

In addition to a strong external magnetic field, a transverse magnetic field perpendicular to the external field is applied to change the direction of the magnetic moment. This transverse magnetic field oscillates at the Larmor frequency of M_o, which enables it to interfere constructively with precession. The net effect is a change in the direction

of M_o, with vector components M_L in the longitudinal (parallel to the external field) direction and M_T in the transverse (perpendicular) direction, as shown in Figure 1.3.[10, 25]

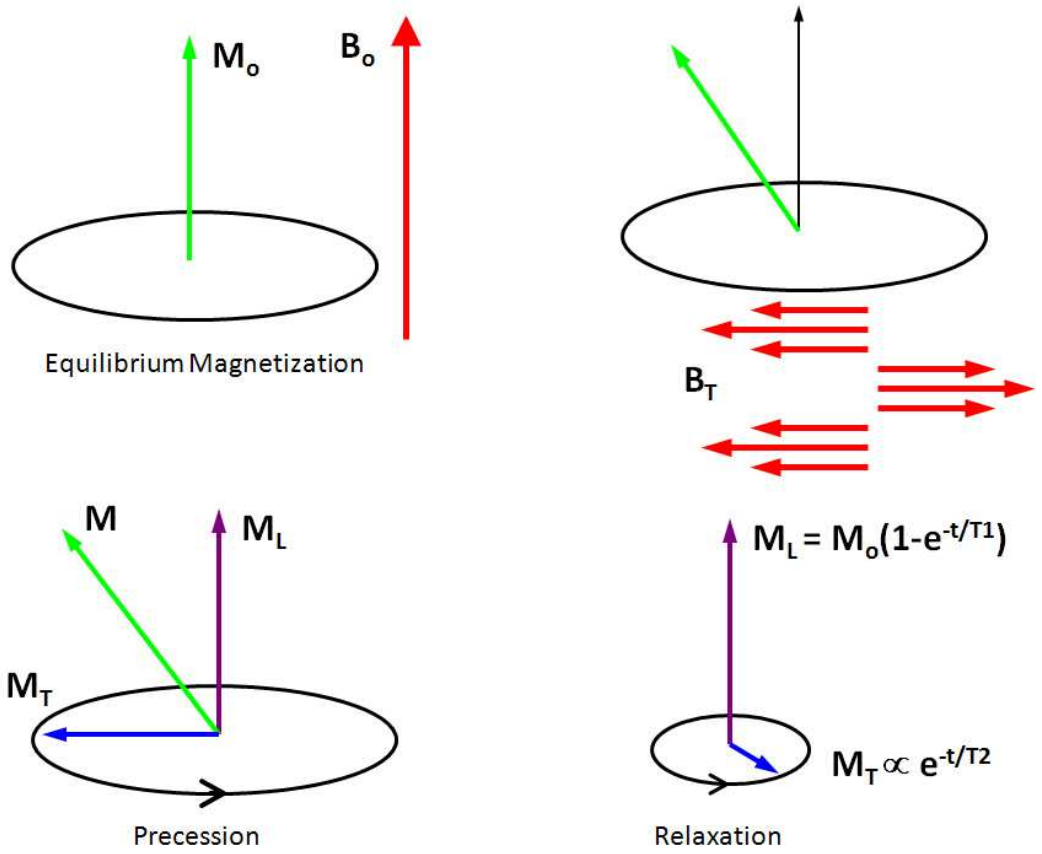

Figure 1.3: MRI excitation and relaxation phenomena. Equilibrium magnetization (M_o) occurs as magnetic dipoles align with the external magnetic field (B_o). Next, a transverse, oscillating magnetic field (B_T) is applied that causes a change in the direction of the equilibrium magnetization. This can be decomposed into a longitudinal (M_L) and a transverse (M_T) vector component. M_T decays and $M_L \rightarrow M_o$ in time as functions of the relaxation parameters, T1 and T2.[10, 25]

In time, M_L will approach the value of M_o due to random thermal motions of the molecule. This process is called spin-lattice relaxation, and the time required for this to occur is called the T1 relaxation time. Additionally, M_T will decay as M_o is regenerated via entropic interactions with other magnetic dipoles. This process is called spin-spin relaxation, and is quantified by the T2 relaxation time. Both the T1 and T2 relaxation times are important parameters used to generate an MR image.[10, 25]

Paramagnetic contrast agents are often introduced in MRI to enhance image contrast between healthy and diseased tissue or to indicate the status of organ function or blood flow.[26] Typical agents include chelates of Gd^{3+}, Fe^{3+}, or Mn^{2+}. Paramagnetic contrast agents function by reducing the relaxation times of local ^{1}H nuclei through magnetic interactions between unpaired electrons and hydrogen nuclei.[26] This causes a local change in contrast, which may be used to distinguish between healthy and pathological tissues.

A detailed description of the physics of magnetic resonance imaging is described in Appendix A.

^{19}F Imaging: In addition to paramagnetic MRI contrast enhancement techniques, contrast agents based on ^{19}F NMR are emerging as an attractive option due to the near-zero background ^{19}F signal, good

biocompatibility of fluorinated compounds, and high gyromagnetic ratio of fluorine.[27, 28] ^{19}F imaging has several benefits over paramagnetic contrast agents. Because fluorine is not commonly found in the body, ^{19}F imaging offers a high signal to noise ratio. Additionally, unlike paramagnetic contrast agents, which modulate the relaxation times of surrounding ^{1}H nuclei, fluorine generates an intrinsic NMR signal.[27] For this reason, it can be imaged directly and superimposed over an anatomical ^{1}H image. Fluorinated contrast agents could be designed that will actively or passively target tissues of interest (e.g. tumors, inflammation), and their location can then be determined with reference to an anatomical MR image that was acquired concurrently. This property suggests that ^{19}F MRI would be similar to PET imaging, although it would not require that the patient be exposed to ionizing radiation and would be much less expensive.

Several studies have validated the concept of ^{19}F MRI contrast agent design. Schwarz et al. used perfluorononane as a gastrointestinal contrast agent due to its biological inertness, immiscibility with water, and high fluorine content.[29] The authors monitored the passage of the perfluorocarbon liquid through the GI tract of a mouse using ^{19}F MRI, rendering a three dimensional model of the GI tract. The authors were

then able to superimpose these images over conventional ^{1}H MR images to provide complimentary anatomical information.[29]

Nanoparticle ^{19}F MRI contrast agents have also been developed with some success. In a study by Du et al., amphiphilic fluoropolymers were synthesized using atom transfer radical polymerization (ATRP) and their micelles were constructed in water.[27] The authors acquired ^{19}F phantom images of the particles in solution, which suggested that they may be useful as novel contrast agents for a variety of biomedical applications.[27]

Because of its unique properties, fluorine is being utilized in a variety of biomedical applications, including imaging agents. Fluorinated compounds have been used in PET imaging, ultrasound imaging, and magnetic resonance imaging and are an interesting candidate for use as a SIMS contrast agent. The overall goal of this work is to develop a fluorinated nanoparticle that is suitable for use as an *in vivo* MRI contrast agent and a SIMS contrast agent.

Chapter 2

Synthesis and Characterization of Fluorinated Nanoparticles for Multimodal Imaging Applications

2.1 Introduction

Nanomaterials have emerged as valuable tools in biomedical imaging techniques, such as magnetic resonance imaging (MRI), fluorescence, and positron emission tomography (PET).[27, 30-35] Some have been designed to serve as multimodal imaging agents, combining seemingly disparate techniques such as fluorescence,[34] photoacoustic tomography (PAT),[35] or positron emission tomography (PET)[30, 32] with magnetic resonance imaging (MRI). Particles have also been designed that combine PET with fluorescence imaging and magnetic resonance imaging capabilities.[20] Combining different imaging modalities into a single contrast agent enables one to capture meaningful images at different levels of spatial resolution from the same sample. Here, the one-step synthesis of a colloidally stable, fluorinated polymeric nanoparticle suitable for secondary ion mass spectrometry (SIMS) imaging and MRI is reported. Fluorine-containing compounds were selected for this application because of fluorine's biological rarity,[29] high ion yield in SIMS,[16] and magnetic activity.[29]

SIMS is a technique that is gaining recognition in the area of high resolution bioimaging. In time of flight SIMS (TOF-SIMS), a sample is bombarded with an electrostatically focused primary ion beam, causing secondary ions to be ejected from the surface. These ions are then

collected in a TOF mass analyzer and a mass spectrum is generated.[36] The primary ion beam can be raster scanned across the sample to record a mass spectrum for each pixel. Ions of interest can be selected from the spectra, and the distribution mapped to produce an image of the sample surface. This technique has been used to quantitatively map the distribution of a variety of biomolecules in tissues and individual cells,[37-42] and can be used as a diagnostic imaging tool to identify cancer biomarkers.[43] Developing a contrast agent that binds to cancer cell epitopes and generates a strong intrinsic SIMS signal (like fluorinated compounds), or enhances the signal of the molecule of interest, would help enhance the ability to detect the presence of specific biomarkers. Recently, this has been done with gold nanoparticles to enhance the signal of cell surface biomolecules.[44, 45]

Fluorinated nanoparticles have also been studied as potential MRI contrast agents.[27, 30, 32, 33, 46-48] The rarity of physiologic fluorine can be exploited to generate highly selective, ^{19}F images that can be superimposed over complimentary ^{1}H images, thus providing an anatomical context for the fluorinated contrast agent.[29, 48, 49] Research in this area has focused on the synthesis of fluorinated nanoparticles using a variety of different approaches. Studies have validated the premise of ^{19}F MRI using nanoemulsions that contain a perfluorocarbon phase.[46, 47, 49-51]

These studies have used materials such as perfluoro-15-crown-5-ether[47, 50, 51] or perfluorooctyl bromide[49, 51], which is emulsified into an aqueous phase using a biocompatible surfactant. Other studies have created novel fluorinated amphiphilic block copolymers that form micelles in aqueous solution.[12, 27, 32, 33] Typically, a living free radical polymerization method is employed to synthesize such amphiphilic block copolymers.[12, 27, 33] This polymer self assembles in water and the resulting suspension is used as the contrast agent.

Developing particles that have the ability to actively or passively target cells or tissues with specific pathologies, such as tumors, could enable one to locate tumors or other sites of inflammation with greater precision using MRI, or analyze biopsied tumor tissue using SIMS. One possible application of this, in the context of tumor imaging, is to develop particles with a long circulation half-life, which could preferentially extravasate through the discontinuous endothelium of the tumor and into the tumor interstitium, where they would accumulate and provide contrast in that region.[12, 52] This phenomenon is known as the enhanced permeability and retention effect, or EPR effect.[53] Another possible method is to functionalize the surface of nanoparticles with targeting agents, such as antibodies or RNA fragments that specifically bind to the

tumor cell epitope.[48, 54] MRI can then be used to locate the tumors *in vivo*, and biopsied tumor tissue could potentially be analyzed using SIMS.

Although current methods to create fluorinated nanoparticles have demonstrated some success, a potential concern is nanoparticle stability. For example, the stability of some micellar nanoparticles and lipid-based emulsions is dependent on the critical micellar concentration (CMC) of the material.[12] Concentration can easily be controlled *in vitro*, but the concentration of the particles might vary greatly when introduced into a physiological environment, which could disrupt the micelle or nanoemulsion stability if the local concentration falls below a critical concentration, which could adversely affect *in vivo* performance. One possible way to overcome this encumbrance is to design a nanoparticle with physical stability that is independent of concentration by introducing a covalent crosslinker. Here, the synthesis and characterization of a novel fluorinated, polymeric nanoparticle contrast agent containing a covalent crosslinker is reported.

2.2 Materials and Methods

Materials: All materials were purchased from Sigma-Aldrich (St. Louis, MO) unless otherwise stated. 1H,H-perfluoro-n-octyl acrylate was purchased from ExFluor Research Corporation (Round Rock, TX). Vazo-

52 was purchased from DuPont (Wilmington, DE). Prior to nanoparticle synthesis, (1,5-N-vinylformamido) ethyl ether was prepared as previously described.[55] Impurities were precipitated out of N-vinylformamide using absolute ethanol and vacuum filtered prior to use. All other reagents were used as received.

Nanoparticle Synthesis: Nanoparticles were synthesized using a free radical polymerization technique. First, 10 µL of 1H,H-perfluoro-n-octyl acrylate, 3.5 µL of N-vinylformamide, 7 µL of (1,5-N-vinylformamido) ethyl ether, and 0.005 g of (E)-2,2'-(diazene-1,2-diyl)bis(2,4-dimethylpentanenitrile) (Vazo-52) were added to absolute ethanol containing 0.018 g/mL polyvinylpyrrolidone (MW approximately 360 kDa). The reagent mixture was sparged for 10 min with argon to remove dissolved oxygen, then heated in a silicone oil bath to 50 ℃ and stirred at approximately 900 rpm. The reaction was carried out under an argon atmosphere for 24 h. The product was then dialyzed against deionized water using a 1 kDa MWCO regenerated cellulose ester dialysis tube for 24 h. The dialysate was changed 5 times to ensure complete solvent exchange. Particle suspensions were then centrifuged twice at 15,000 rpm for 45 min. The pellet was collected each time and resuspended in deionized water. The reaction scheme is shown in Figure 2.1.

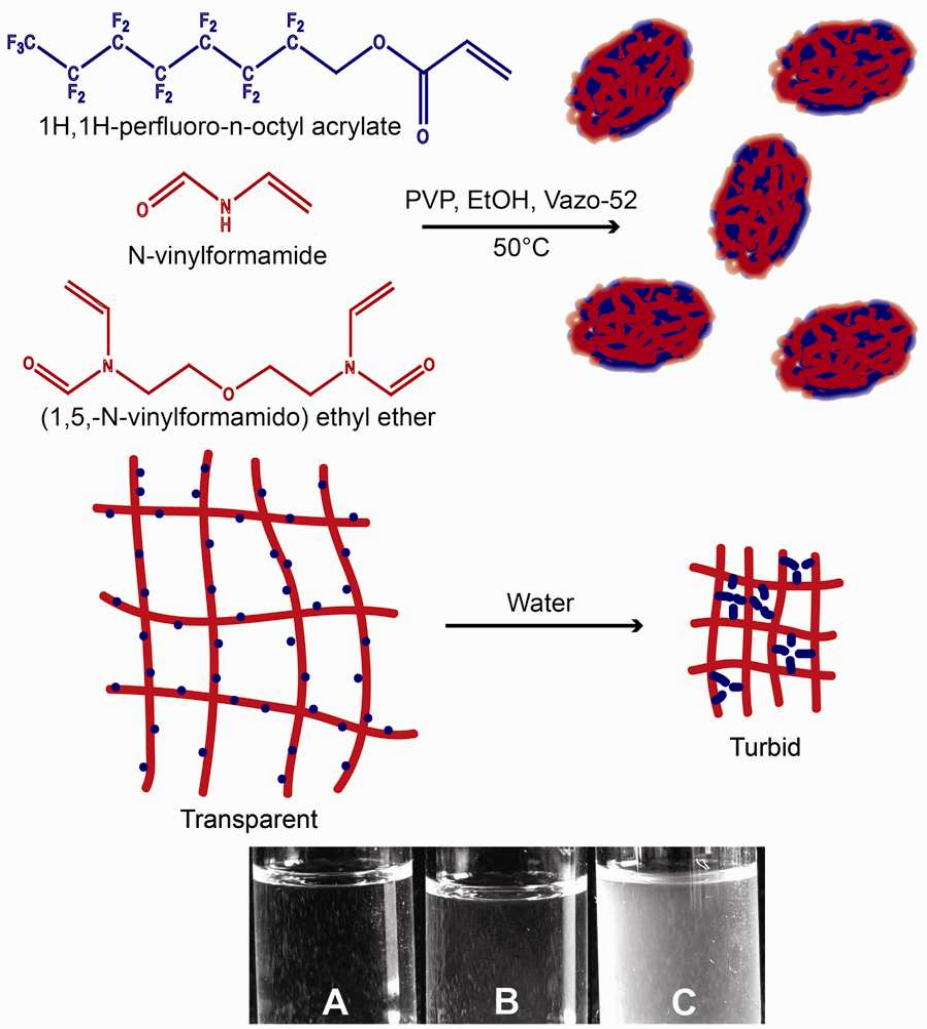

Figure 2.1: The top scheme depicts the nanoparticle synthesis. The middle scheme depicts the proposed interaction between fluorinated side chains (blue) as the product is transferred from ethanol to water and transitions from transparent to turbid. The photograph inset shows (A) reagent mixture prior to reaction, (B) product in ethanol after reaction, and (C) nanoparticle suspension in water after dialysis. (PVP: polyvinylpyrrolidone.)

Characterization of Nanoparticles: The size and zeta potential of the nanoparticles were determined using dynamic light scattering (ZetaPals, Brookhaven Instruments). All measurements were taken 5 times. Measurements are reported as the mean ± standard uncertainty. ESEM experiments were performed using an FEI Quanta field emission environmental scanning electron microscope. Samples were prepared by decanting a small volume of nanoparticles suspended in deionized water onto a polished silicon wafer and allowing the water to evaporate under a fume hood. Samples were sputter coated with 5 nm of gold prior to imaging. All samples were analyzed using an acceleration voltage of 10 keV under high vacuum.

Time of Flight Secondary Ion Mass Spectrometry (TOF-SIMS): TOF-SIMS was used to analyze the surface chemistry of the nanoparticles (Ion-TOF IV). Samples were prepared by decanting a small volume of nanoparticles suspended in deionized water onto a polished silicon wafer and allowing the water to evaporate under a fume hood. TOF-SIMS experiments were performed on an Ion-TOF IV instrument equipped with both Bi (Bi_n^+, where n = 1 to 7) and SF_5^+ primary ion beam cluster sources. The analysis source was a pulsed, 25 keV bismuth cluster ion source (Bi_3^+), which bombarded the surface at an incident angle of 45

degrees to the surface normal. The target current was maintained at approximately 0.3 pA (± 10%) pulsed current with a raster size of 200 µm x 200 µm for all experiments. Both positive and negative secondary ions were extracted from the sample into a reflectron-type time of flight mass spectrometer. The secondary ions were then detected by a microchannel plate detector with a post-acceleration energy of 10 kV. A low energy electron flood gun was utilized for charge neutralization in the analysis mode. Each spectrum was averaged over a 60 s time period, with a cycle time of 100 µs. These conditions resulted in accumulated Bi_3^+ ion doses that were well below 10^{13} ions/cm^2.

FTIR Reflection Spectroscopy: FTIR spectroscopy was used to qualitatively determine the identity of functional groups present within the nanoparticles (Smiths Illuminate FTIR Microscope). All experiments were done on a diamond attenuated total reflectance objective microscope accessory. Reported spectra are the average of 128 scans.

Solid State ^{19}F-NMR Spectroscopy: The solid-state NMR (ssNMR) spectra were obtained on a 3-channel Chemagnetics spectrometer operating at 284.0 MHz for ^{19}F and 301.9 MHz for ^{1}H using an ^{1}H/^{19}F probe. The sample was packed in a 4 mm zirconia rotor with Torlon™

endcaps and Vespel™ drivetips and rotated at 10,000 kHz. The NMR spectrum was obtained using H-F cross polarization and a sweep width of 100 kHz. A total of 1024 scans were obtained with a dwell time of 10 µs. The chemical shift reference was set at -121.1 ppm using Teflon™ Interference from the Teflon™ endcaps was not subtracted because it was negligible under these conditions.

2.3 Results and Discussion

Fluorinated nanoparticles were synthesized using a single step, free radical polymerization method and then precipitated in water. In this method, N-vinylformamide, (1,5-N-vinylformamido) ethyl ether, and 1H,H-perfluoro-n-octyl acrylate were added to a solution of polyvinylpyrrolidone (PVP) in ethanol (Figure 2.1). Vazo-52 was added as an initiator, and the solution was sparged with argon. The reaction was carried out at 50 ºC for 24 hours. Particles were prepared without PVP under the same conditions to serve as a control group. These particles were larger than the particles prepared in the presence of PVP and were not used in further analysis. The product was then dialyzed against deionized water to induce particle precipitation, and then centrifuged and resuspended twice in water (Figure 2.1).

The nanoparticles had a size distribution with maxima at 250 nm and 700 nm according to dynamic light scattering. After adding Tween-20 (final concentration: 5.0×10^{-4} g/mL) and sonicating for 4 h, the distribution maxima shifted to 250 nm and 575 nm (Figure 2.2). Environmental scanning electron microscopy (ESEM) imaging suggested that the particles were substantially smaller than 500 nm (Figure 2.2). The disparity between the ESEM and the DLS data could be partially due to swelling of the particles in aqueous medium, but is most likely due to flocculation occurring in water, which would increase the particle size observed by DLS. DLS measurements taken of the product in ethanol after polymerization were indistinguishable from the background, suggesting that the product was soluble. After precipitation in water and solvent exchange, particles demonstrated excellent colloidal stability, and showed only minor settling when left undisturbed at room temperature for more than five months. This settling was easily reversed by lightly shaking the vial for several seconds.

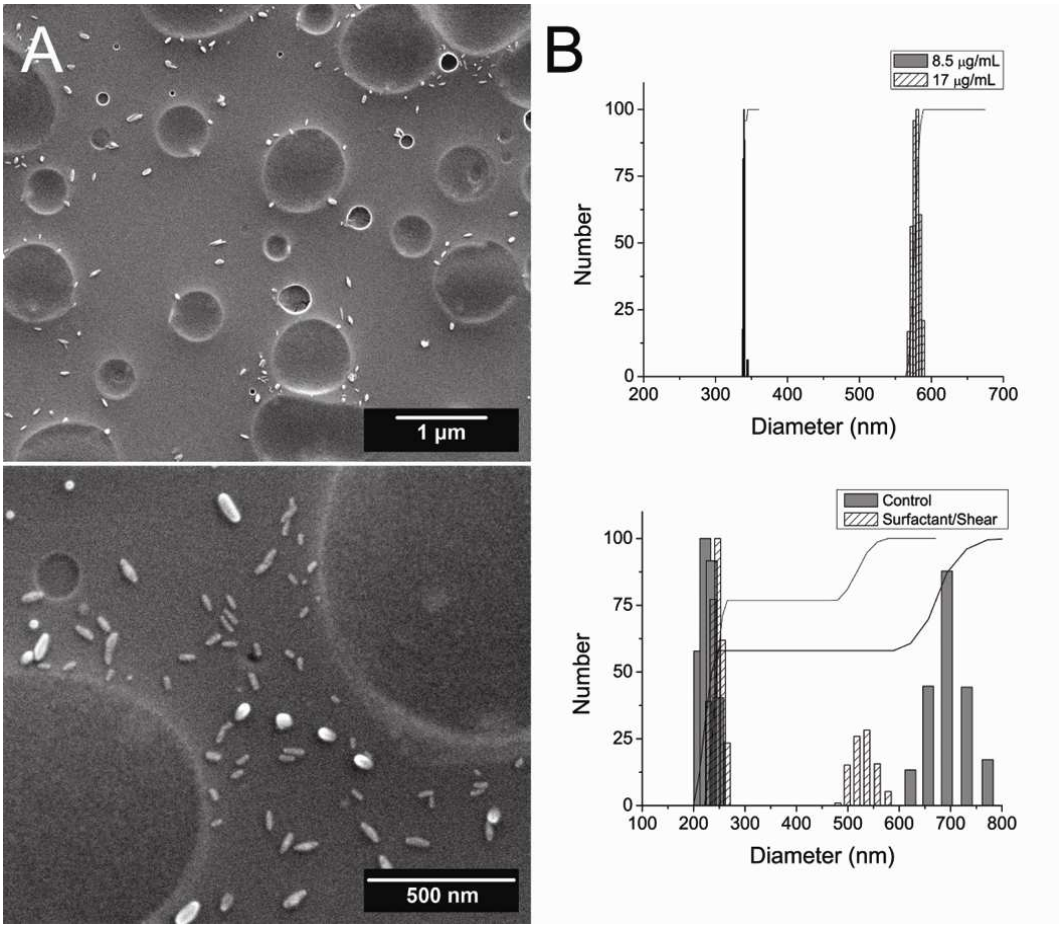

Figure 2.2: (A) ESEM images of the fluorinated nanoparticles, which appear as white spheres and ellipsoids. Image analysis using Image-Pro software revealed a mean particle size of 47.0 nm ± 3.6 nm (95% confidence level). (B) Dynamic light scattering measurements of fluorinated nanoparticles under different conditions; (top) size as a function of nanoparticle concentration, (bottom) effect of Tween-20 and sonication on particle size. Under shear and in the presence of the surfactant, particle flocculation is reduced. The lines represent the cumulative distribution function.

Fourier Transform Infrared Spectroscopy (FTIR) was used to determine the functional groups present in the particles (Figure 2.3). The spectra for the nanoparticles showed bands corresponding to both amide I

(1670 cm^{-1} – 1650 cm^{-1}) and amide III (1315 cm^{-1} – 1250 cm^{-1}) peaks. The spectra also showed a second peak in the carbonyl region (1690 cm^{-1} – 1760 cm^{-1}), as well as peaks in the ester region (1080 cm^{-1} – 1300 cm^{-1}), which were due to the presence of the fluorinated ester group. These peaks were present in the spectra from particles prepared both with and without PVP surfactant, indicating that they originated from the particles themselves and were not solely an artifact from the γ-lactam groups present in residual PVP.

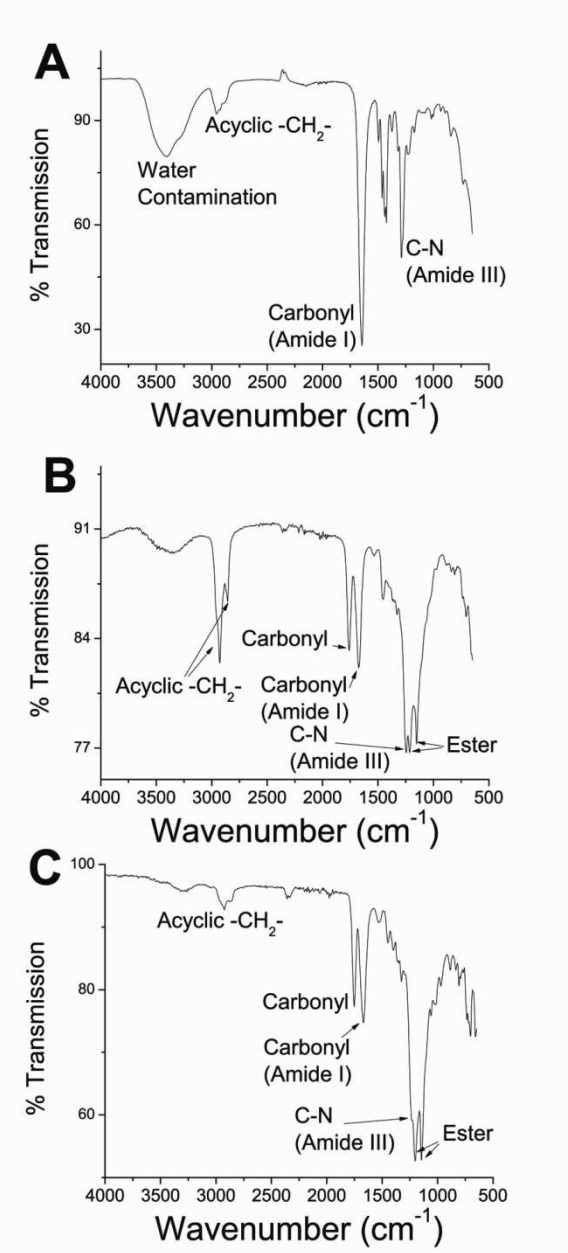

Figure 2.3: FTIR spectrum of fluorinated nanoparticles. The spectrum for (A) PVP is compared to (B) particles synthesized in the presence of PVP and (C) particles synthesized without PVP. Both spectra (B) and (C) show amide I and amide III peaks, suggesting that N-vinylformamide (NVF) is incorporated into the particles. Spectra (B) and (C) also show carbonyl peaks and ester peaks, suggesting the presence of the fluorinated ester acrylate group.

TOF-SIMS experiments suggested the presence of fluorinated groups on the surface of the particles (Figure 2.4), indicating they would be a suitable agent for cellular imaging applications. SIMS has a sampling depth of approximately 1 nm in polymeric materials,[56-58] suggesting that some of the fluorinated side chains were present on the surface of the particles. Spectra also indicated the presence of nitrogen-containing groups, which could be from the N-vinylformamide side chain, the (1,5-N-vinylformamido) ethyl ether crosslinker, or residual PVP surfactant. Regardless of their source, the nitrogen-containing groups provided the particles with a hydrophilic surface character, which may contribute to their aqueous stability.

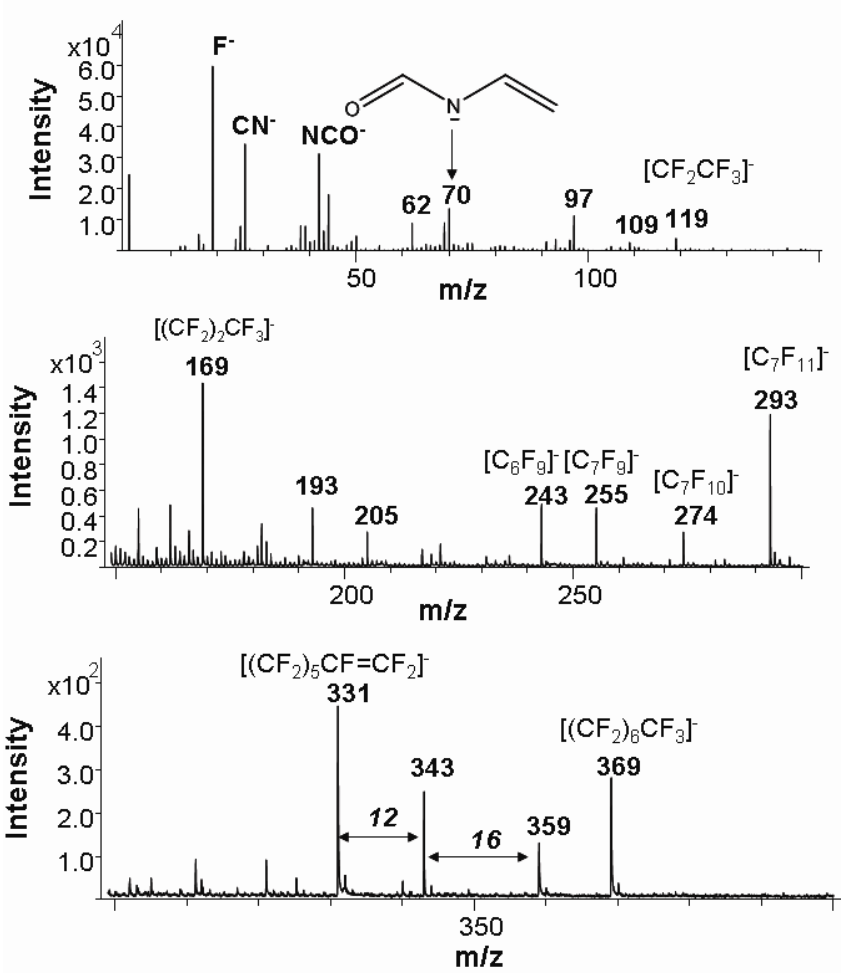

Figure 2.4: Negative secondary ion mass spectra for nanoparticle samples suggest the presence of nitrogen-containing functional groups and fluorinated groups on the surface of the particles.

The presence of fluorinated groups on the surface of the particles could help explain the disparity between the particle sizes measured with dynamic light scattering and the sizes suggested from the ESEM experiments. The fluorinated groups are extremely hydrophobic, and it is probable that their presence on the particles' surface would induce

flocculation due to hydrophobic interactions. This phenomenon would be in competition with the repulsive effects of the hydrophilic groups on the particles' surface. DLS experiments showed changes in measured particle size as particle concentration was varied, which suggests that flocculation was occurring (Figure 2.2). Additionally, sonication and the addition of Tween-20 (final concentration: 5.0×10^{-4} g/mL) were shown to decrease the effect of flocculation.

Solid-state ^{19}F-NMR (ssNMR) was used to help further elucidate the structure of the particles and validate their use as MRI contrast agents (Figure 2.5). The locations of the peaks were consistent with the presence of two different fluorine-containing sites within the fluorinated group. The peak at -82.1 ppm originates from CF_3 fluorine and the one at -122.8 from CF_2 fluorine, which is overlapped with spinning sidebands. This is consistent with the structure of the 1H,H-perfluoro-n-octyl acrylate monomer. The spectrum suggests that *in vivo* studies will require selective excitation due to the different fluorine chemical shifts present in the particles.[11, 27]

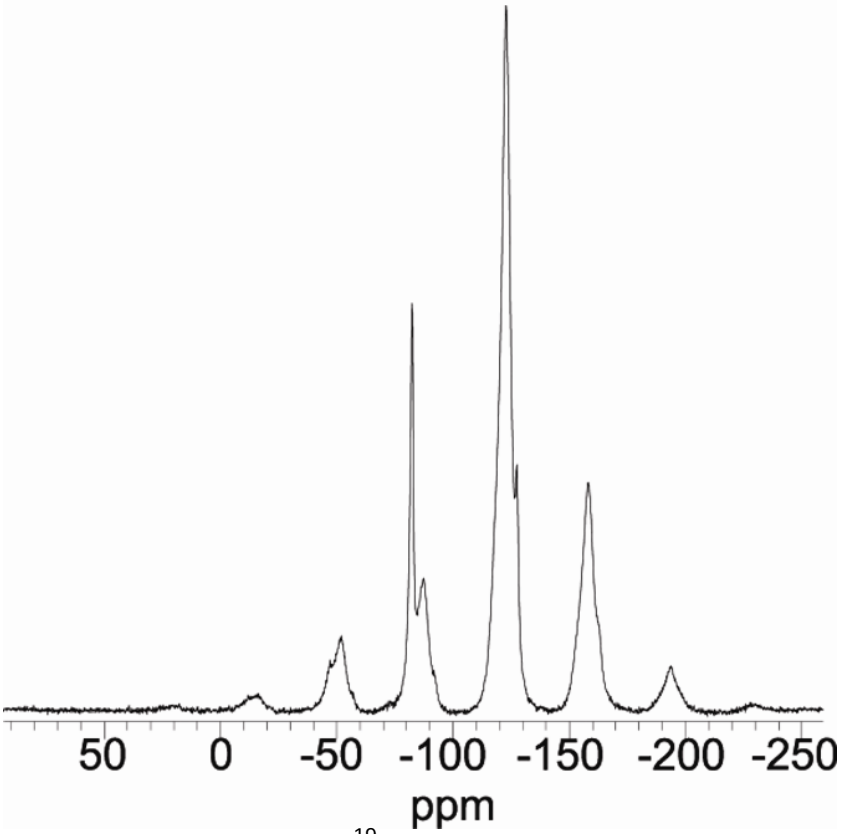

Figure 2.5: The solid state ^{19}F NMR spectrum of the fluorinated nanoparticles reveals peaks consistent with the presence of two different fluorine-containing sites in the fluorinated group. The peak at -82.1 ppm originates from CF_3 fluorine, and the one at -122.8 ppm from CF_2 fluorine. The CF_2 peak is surrounded by spinning sidebands.

Developing fluorinated nanoparticles for multimodal ^{19}F-MRI and SIMS imaging that possess intrinsic colloidal stability represents a largely unexplored research area. Here, particles less than 500 nm in diameter were synthesized using free radical polymerization, followed by precipitation. Secondary ion mass spectrometry was used to determine the chemical properties of the particles' surface, which will greatly impact

their colloidal stability and cytotoxicity. The strong fluorine signal indicated that the particles would be suitable for SIMS imaging applications. We hypothesize that the inclusion of hydrophilic monomers in the polymerization process enhances their colloidal stability and helps prevent irreversible agglomeration that might otherwise occur due to the fluorinated groups. Hypothetically, this technology could be extended to include degradable monomers or crosslinkers,[59, 60] or PEG acrylates to improve their properties. Ongoing studies will evaluate the performance of the nanoparticles as MRI contrast agents both *in vitro* and *in vivo*, as well as the suitability of the particles for cellular level imaging using SIMS.

Chapter 3

Analysis of a Nanoparticle Contrast Agent Using Small Angle Neutron Scattering (SANS)

3.1 Introduction

Magnetic resonance imaging (MRI) is a powerful diagnostic imaging tool that is both noninvasive and nondestructive. Paramagnetic contrast agents, such as gadolinium chelates, are often used to accelerate proton relaxation and can be employed to reveal features that might otherwise be obscured as a result of similarities in the relaxation times of adjacent tissues.[26, 27, 31] Although MRI has been an effective diagnostic tool, often the contrast changes are ambiguous and difficult to interpret. Additionally, the biological impact of traditional Gd^{3+} ion chelates, particularly macromolecular agents, is poorly understood.[61] To overcome these challenges, there has been intense interest in developing contrast media containing biologically rare, magnetically active nuclei, such as fluorine.[27, 30, 32, 33, 46-48] Fluorinated materials are an excellent choice for this application because of fluorine's biological rarity and magnetic properties, and because of the excellent biocompatibility demonstrated by fluorinated colloids.[1, 2, 28] In principle, the rarity in physiological fluorine can be exploited to generate highly-selective ^{19}F images that can be superimposed over complimentary ^{1}H images, providing an anatomical context for the fluorinated contrast agent.[29, 49] Additionally, developing nanoparticle-based contrast agents that have the ability to actively or passively target tissues with specific pathologies, such as tumor tissue

and atherosclerotic plaques, could enable clinicians to better diagnose such conditions using MRI.

A specific example of an active targeting strategy involves conjugating nanoparticles with ligands that specifically bind cellular antigens associated with a pathological state of interest. This technique may amplify the specificity of nanoparticles to the target site.[62, 63] A potential passive targeting strategy that may be specifically applicable to tumor targeting exploits the anatomical and physiological abnormalities of tumor vasculature that compromise lymphatic drainage and cause leakage of macromolecular agents and nanoparticles into the tumor interstitium. This phenomenon is known as the enhanced permeability and retention effect, or EPR effect, and can potentially be exploited by controlling the nanoparticle size.[63-67]

This study aims to develop fluorinated nanoparticles that exhibit magnetic activity and therefore might be suitable for biomedical imaging using ^{19}F-MRI.[63] Nanoparticles were synthesized using two different fluorinated monomers, which were compared using neutron scattering and ^{19}F-NMR. Amide groups on the nanoparticles were then hydrolyzed to their corresponding amines at high pH. Linear polymers prepared without the covalent crosslinker were hydrolyzed as a comparison. The results indicated that both particle types were approximately 500 nm or smaller in

diameter, and that they generated a significant ^{19}F-NMR signal, which suggested they might be suitable for imaging using ^{19}F-MRI. Additionally, FTIR spectra indicated that amide groups on the particles were hydrolyzed to amines at high pH, which suggested they can be conjugated with ligands for active targeting strategies.

3.2 Materials and Methods

Materials: All materials were purchased from Sigma-Aldrich (St. Louis, MO) unless otherwise stated. 1H,H-perfluoro-n-octyl acrylate was purchased from ExFluor Research Corporation (Round Rock, TX). 2-(allyl)hexafluoroisopropanol was purchased from Matrix Scientific (Columbia, SC). Vazo-52 was purchased from DuPont (Wilmington, DE). Dialysis membranes were purchased from Spectrum Labs (Rancho Dominquez, CA). Prior to nanoparticle synthesis, (1,5-N-vinylformamido) ethyl ether was synthesized as previously described.[55] Impurities were precipitated out of N-vinylformamide using absolute ethanol prior to use. All other reagents were used as received.

Synthesis of Fluorinated Nanoparticles: Nanoparticles were synthesized using a free radical polymerization technique as described previously.[68] First, 20 µL of N-vinylformamide, 20 µL of (1,5-N-vinylformamido) ethyl

ether, and 20 µL of the fluorinated monomer (either 1H,H-perfluoro-n-octyl acrylate, or 2-(allyl)hexafluoroisopropanol) were dissolved in absolute ethanol containing 0.015 mg/mL polyvinylpyrrolidone (PVP) as a surfactant (MW approximately 360 kDa). Next, 6.9 mg of (E)-2,2'-(diazene-1,2-diyl)bis(2,4-dimethylpentanenitrile) (Vazo-52) were added to the solution as an initiator (Figure 3.1).

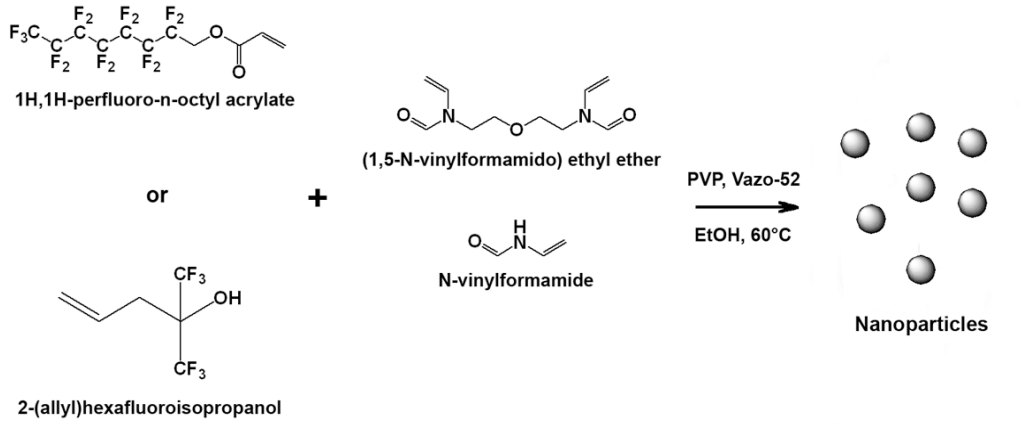

Figure 3.1: Diagram of the reaction scheme. For each batch, one of the fluorinated monomers was reacted with (1,5-N-vinylformamido) ethyl ether and N-vinylformamide to generate nanoparticles. The reaction was carried out in ethanol at 60℃ using Vazo-52 as an initiator and polyvinylpyrrolidone (PVP) as a surfactant. For the analogous polymers, the same reaction scheme was used, but without the addition of the (1,5-N-vinylformamido) ethyl ether crosslinker or the PVP surfactant.

The reagent mixture was then sparged with argon for 10 minutes to remove dissolved oxygen, then heated in a silicone oil bath to 60℃ and stirred at approximately 900 RPM. The reaction was carried out

isothermally under an argon atmosphere for 24 hours. The product was then dialyzed against deionized water using a 1 kDa MWCO regenerated cellulose ester dialysis tube (Spectrum Laboratories, Inc., Rancho Dominquez, CA) for 24 hours. The dialysate was changed at least 5 times to ensure complete solvent exchange. Linear polymers were synthesized analogously, but without the addition of (1,5,-N-vinylformamido) ethyl ether crosslinker or PVP surfactant. Particles were then further purified by centrifugation for 1 hour at 18,000 rpm. Each centrifugation cycle was repeated at least 3 times.

For the hydrolysis step, particle and polymer suspensions were flash-frozen in liquid nitrogen and then lyophilized. Samples were resuspended in 1 M $NaOH_{(aq)}$ and sonicated for 1 hour at ambient temperature, as described previously.[59] The pH of each solution was then titrated to approximately 7 using 1 M $HCl_{(aq)}$, and the suspensions were dialyzed against deionized water (MWCO 100 Da) for at least 24 hours to remove salt and hydrolysis byproducts. Dialysate was changed at least 3 times. The hydrolyzed particles and polymers were then flash-frozen in liquid nitrogen and lyophilized prior to analysis with FTIR.

Neutron Scattering: SANS experiments were carried out on the NG7 30 m SANS instrument at the NIST Center for Neutron Research (NCNR) in

Gaithersburg, MD. Neutrons of wavelength $\lambda = 6$ Å with a distribution of $\Delta\lambda/\lambda = 10$ % were incident on samples held in quartz cells. Three different sample to detector distances were used to give an overall q range of 0.0038 Å < q < 0.37 Å, where $q = (4\pi/\lambda)\sin(\theta/2)$ is the magnitude of the scattering vector. Sample scattering was corrected for background and empty cell scattering, and the sensitivities of individual detector elements were normalized. The corrected data sets were circularly averaged and placed on an absolute scale using software supplied by the NCNR.[69]

USANS experiments were carried out on the BT54 perfect crystal diffractometer (PCD) at the NCNR using the same samples described above. The overall q range was 3.8×10^{-5} Å < q < 0.002 Å. All data were reduced and analyzed using software provided by the NCNR.[69] Here, only slit-smeared data are shown.

Samples for all neutron scattering experiments were prepared using D_2O as a solvent, thus the scattering length density of the solvent was 6.3×10^{-6} Å^{-2}. Particle densities were approximated using a weighted average of the neat monomer densities. Scattering length densities of the particles were calculated using the NCNR scattering length density calculator[70] with atomic scattering lengths obtained from V.F. Sears.[71]

TEM Imaging: TEM images were acquired on a Philips CM300FEG TEM

(C_s = 1.2 mm) operated at 300 kV using a 10.8 mrad objective aperture semiangle. Samples were drop-mounted onto silicon-supported 25 nm thermal SiO_2 membranes (Dune Sciences NG01-011A) and allowed to dry in air for 24 hours before imaging. Samples were imaged using a Gatan GIF-200 in energy filtered mode using a 10 eV acceptance slit. To increase signal to noise ratios, the images were constructed from a series of 100, 0.5 second exposures, which were then aligned and summed to produce the final image.

Fourier Transform Infrared Spectroscopy: FTIR was used to determine the effects of hydrolysis on the functional groups present within the nanoparticles (Smiths Illuminate FTIR Microscope). After lyophilization, hydrolyzed and non-hydrolyzed samples were resuspended in deionized water by sonicating in an ultrasonication bath for one hour. Particle and polymer suspensions were then decanted onto a gold-plated microscope slide and allowed to dry at ambient conditions under a chemical hood. FTIR spectra were then collected from the resultant polymer and particle films. All experiments were conducted on a diamond attenuated total reflectance objective microscope accessory. Reported spectra are the average of 128 scans.

^{19}F-NMR Spectroscopy: ^{19}F spectra were acquired on a Bruker DRX 400 MHz NMR equipped with a QNP probe at The University of Kansas. The samples were suspended in D_2O and the spectrometer was locked to this solvent during the experiments. All samples were recorded with a sweep width of 99 ppm, a transmitter offset of -80 ppm and a 1 second delay. Spectra were collected with 16 scans on the particles synthesized with the 1H,H-perfluoro-n-octyl acrylate monomer and 64 scans were used for the particles synthesized using the 2-(allyl)hexafluoroisopropanol monomer.

3.3 Results

Small Angle Neutron Scattering: Fluorinated nanoparticles were prepared using a method similar to one described previously.[68] After purification, samples were suspended in D_2O and analyzed using SANS and USANS at several different concentrations. The scattering length density values for particles prepared with each of the fluorinated monomers are given in Table 3.1.

Table 3.1: Scattering Length Densities of Fluorinated Nanoparticles

Monomer	Estimated Particle Density (g/cm^3)	Scattering Length Density ($Å^{-2}$)
1H,1H-perfluoro-n-octyl acrylate	1.30	3.00×10^{-6}
2-Allyl hexafluoroisopropanol	1.15	2.73×10^{-6}

Non-linear least-squares model fitting was performed using Schulz-distributed spheres of uniform scattering length density, given by the normalized Schulz distribution:

$$f(R) = \frac{(z+1)^{(z+1)} x^z}{R_{avg}\Gamma(z+1)} \exp[-(z+1)x]$$

where R_{avg} is the mean radius of the particles, and $x = R/R_{avg}$, z is a function of the polydispersity, $p = \sigma/R_{avg}$, and $z = 1/p^2 - 1$, σ is the standard deviation of the distribution, and Γ(z+1) is the gamma function. For a typical SANS experiment, the SANS intensity is given by:

$$I(q) = \phi V_p \Delta\rho^2 P(q) S(q) + b$$

where φ is the particle volume fraction, V_p is the particle volume, Δρ is the difference between the scattering length density of the particles and the scattering length density of the solvent ($\rho_p - \rho_s$), and b is the incoherent background scattering intensity. The function P(q) is the intraparticle form factor averaged over the Schulz distribution, and S(q) is the interparticle interference factor, which is equal to 1 in the case of non-interacting particles. The particles were confirmed to be non-interacting by measuring at several dilutions. Combining this equation with the normalized Schulz distribution yields:

$$I(q) = \left(\frac{4\pi}{3}\right)^2 \left(\frac{\phi}{\langle V \rangle}\right) \Delta\rho^2 \int_0^\infty f(R) R^6 F^2(qR) dR$$

where, <V> is the average volume of a particle. The function F is the scattering amplitude of a sphere, and is given by:

$$F(x) = \frac{[\sin(x) - x\cos(x)]}{x^3}$$

The average volume, <V>, is calculated using the 3rd moment of R and is given by:

$$\langle V \rangle = \frac{4\pi}{3} (R_{avg})^3 \frac{(z+3)(z+2)}{(z+1)^2}$$

For the particles prepared using the 1H,1H-perfluoro-n-octyl acrylate monomer, the USANS data were initially fit to obtain the size and polydispersity of the particles. For the smaller concentrations (concentrations less than 1 mg/mL), the polydispersity was held at the value calculated from the most concentrated sample. The SANS data were also fit using the parameters calculated from the USANS data, although the background and the volume fraction parameters were relaxed. The model was then fit to both the USANS and the SANS data simultaneously to optimize the fit. The spectra are shown in Figure 3.2, and the model parameters are listed in Table 3.2. The model suggests that the particles are between 390.1 nm ± 4.4 nm and 413.1 nm ± 2.6 nm

in diameter with a polydispersity of 0.5218. The discrepancies between the volume fractions calculated for the USANS and SANS data for each concentration could be due to small amounts of separation that occurred while the samples were waiting for analysis on the SANS instrument.

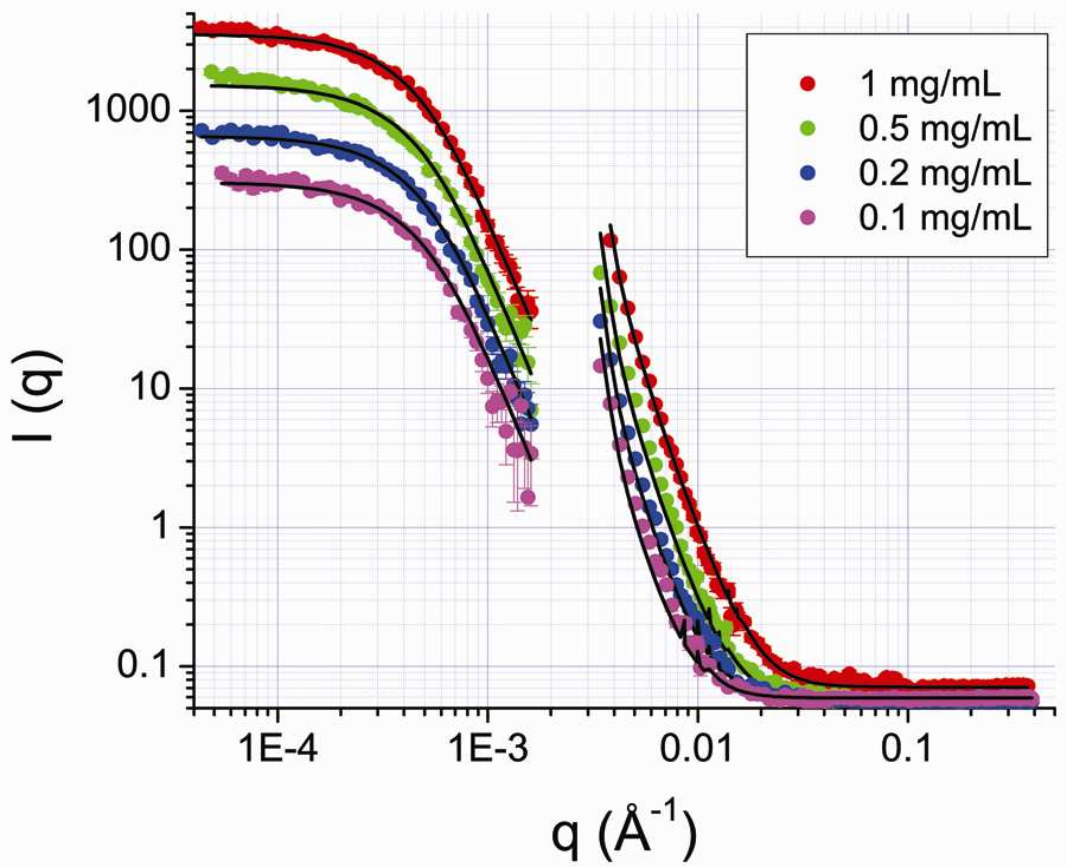

Figure 3.2: USANS and SANS spectra of particles prepared with 1H,1H-perfluoro-n-octyl acrylate monomer. Particles were dispersed in D_2O without surfactant at various concentrations. Data were fit using a Schulz sphere analytical model. The model suggests that the particles are between 290 and 414 nm in diameter with a polydispersity of approximately 0.52.

Table 3.2: Model parameters for nanoparticles prepared with 1H,1H-perfluoro-n-octyl acrylate monomer

	1 mg/mL		0.5 mg/mL	
Parameter	SANS	USANS	SANS	USANS
Volume Fraction	$2.99 \times 10^{-3} \pm 2.8 \times 10^{-5}$	$1.32 \times 10^{-3} \pm 1.4 \times 10^{-5}$	$1.30 \times 10^{-3} \pm 1.3 \times 10^{-5}$	$3.54 \times 10^{-4} \pm 4.1 \times 10^{-6}$
Mean Diameter (nm)	413.1 ± 2.6		410.6 ± 2.8	
Polydispersity	0.522		0.522	
Background (cm^{-1} sr^{-1})	0.071		0.057	

	0.2 mg/mL		0.1 mg/mL	
Parameter	SANS	USANS	SANS	USANS
Volume Fraction	$5.92 \times 10^{-4} \pm 6.5 \times 10^{-6}$	$1.41 \times 10^{-4} \pm 1.9 \times 10^{-6}$	$2.88 \times 10^{-4} \pm 4.8 \times 10^{-6}$	$6.03 \times 10^{-5} \pm 1.1 \times 10^{-6}$
Mean Diameter (nm)	399.1 ± 3.0		390.1 ± 4.4	
Polydispersity	0.522		0.522	
Background (cm^{-1} sr^{-1})	0.056		0.059	

Error is equal to 1 standard deviation of the fitted value. Values without reported error were held exact during model convergence.

For the 2-(allyl)hexafluoroisopropanol monomer, only spectra obtained for concentrations of 1 mg/mL and 0.5 mg/mL were analyzed due to insufficient scattering at lower concentrations. Only the USANS spectra were used in the analysis of 2-(allyl)hexafluoroisopropanol because the SANS data were too noisy and the expected particle size was within the range suitable for USANS measurements. The model was fit to each data set individually, and then to both concentrations simultaneously while holding the polydispersity from the highest concentrated sample constant to minimize the degrees of freedom and to ensure a consistent fit with both data sets. In the spectra for the particles prepared with the 2-

(allyl)hexafluoroisopropanol monomer, the data were too noisy to accurately determine both the particle size and the polydispersity, so the polydispersity was held at 0.5, which is close to the value obtained for the particles prepared with the 1H,H-perfluoro-n-octyl acrylate monomer. The spectra for these particles are shown in Figure 3.3, and the model parameters are listed in Table 3.1. The model suggests an average particle size of 281.2 nm ± 16.4 nm.

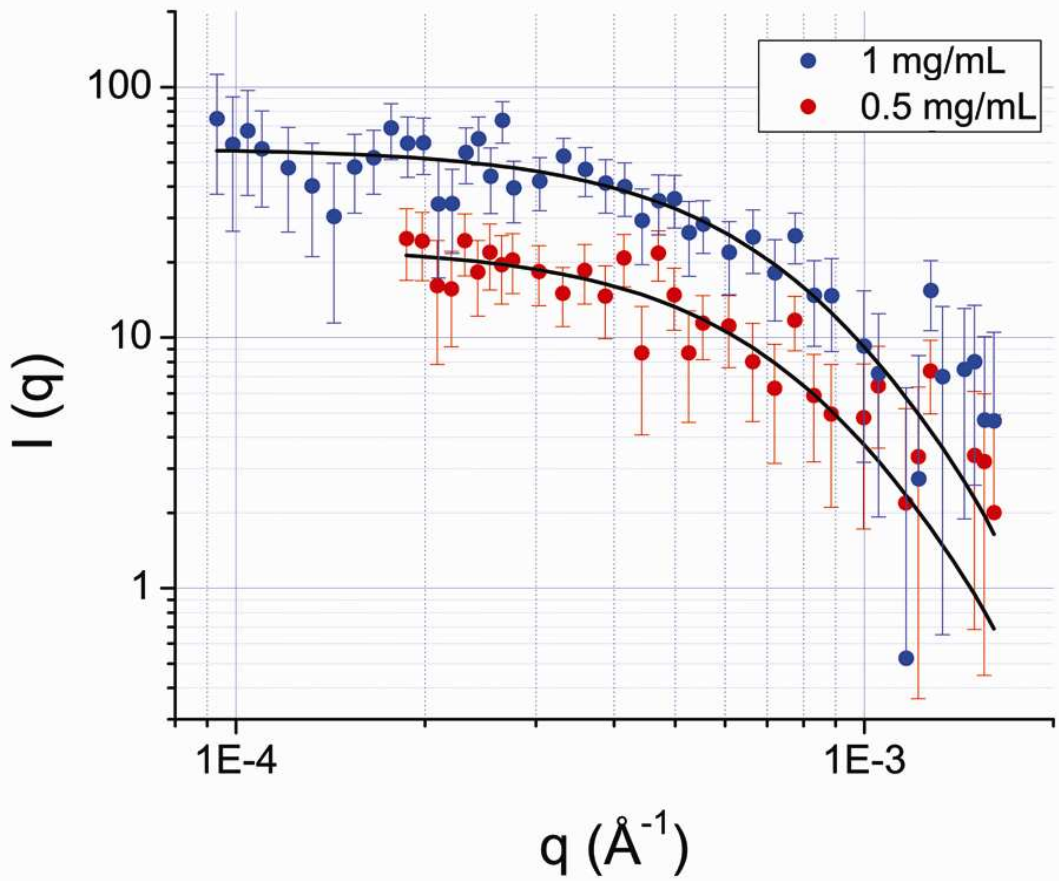

Figure 3.3: USANS spectra of particles prepared with 2-(allyl)hexafluoroisopropanol monomer. Particles were dispersed in D_2O without surfactant at concentrations of 1 mg/mL and 0.5 mg/mL. Data were fit using a Schulz sphere analytical model. The model suggests that the particles are approximately 282 nm in diameter. The polydispersity was held to 0.5 due to the noisiness of the data.

Table 3.3: Model parameters for nanoparticles prepared with 2-allyl hexafluoroisopropanol monomer

Parameter	1 mg/mL	0.5 mg/mL
Volume Fraction	$1.62 \times 10^{-3} \pm 1.5 \times 10^{-4}$	$6.56 \times 10^{-4} \pm 6.2 \times 10^{-5}$
Mean Diameter (nm)	281.2 ± 16.4	
Polydispersity	0.5	
Background (cm^{-1} sr^{-1})	0.218	

Error is equal to 1 standard deviation of the fitted value. Values without reported error were held exact during model convergence.

Transmission Electron Microscopy: The sizes of the fluorinated nanoparticles were further corroborated by the TEM images (Figure 4), which show particles prepared with the1H,H-perfluoro-n-octyl acrylate monomer (Panel A) that are less than 400 nm in diameter. Panel B shows particles prepared with the 2-(allyl)hexafluoroisopropanol monomer that are less than 500 nm in diameter. The observed particle sizes corroborate the neutron scattering data. This suggests that the particles might be useful as a passive targeting agent for tumor imaging.

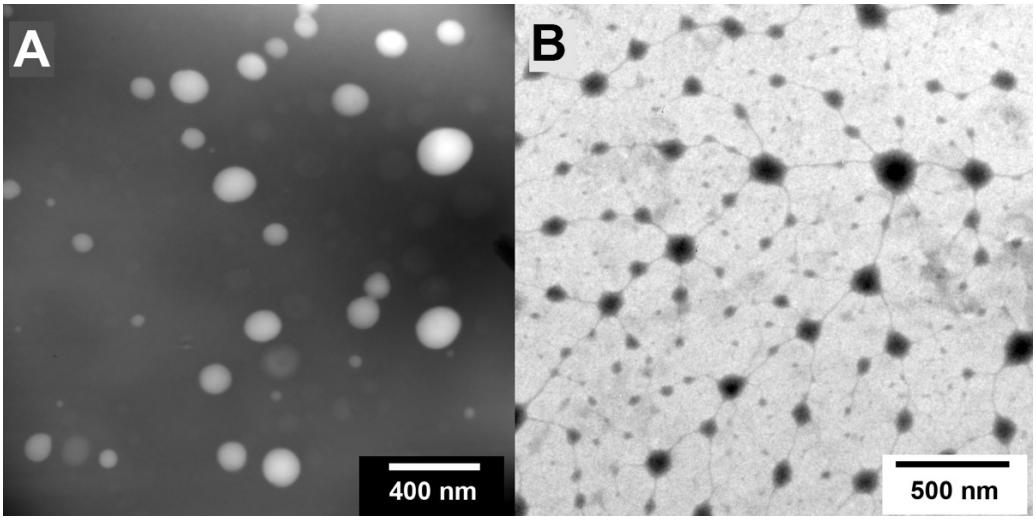

Figure 3.4: TEM Image of particles prepared with 1H,H-perfluoro-n-octyl acrylate monomer (A) and 2-(allyl)hexafluoroisopropanol monomer (B).

Fourier Transform Infrared Spectroscopy: Nanoparticles were analyzed using FTIR to determine the suitability of the particles for chemical modification and conjugation strategies. Analogous polymers prepared without the (1,5-N-vinylformamido) ethyl ether crosslinker or the PVP

surfactant were also analyzed as a comparison. The ability to hydrolyze the amide to an amine could enable one to conjugate a carboxyl terminated targeting ligand to the particles or polymers to facilitate active targeting of pathological tissue. This can be done with simple chemistry that is well described in the literature.[20, 72] Particles prepared using the 1H,H-perfluoro-n-octyl acrylate monomer (Figure 3.5, Panel A) showed evidence of hydrolysis of both the formamide group and of the perfluorinated ester.

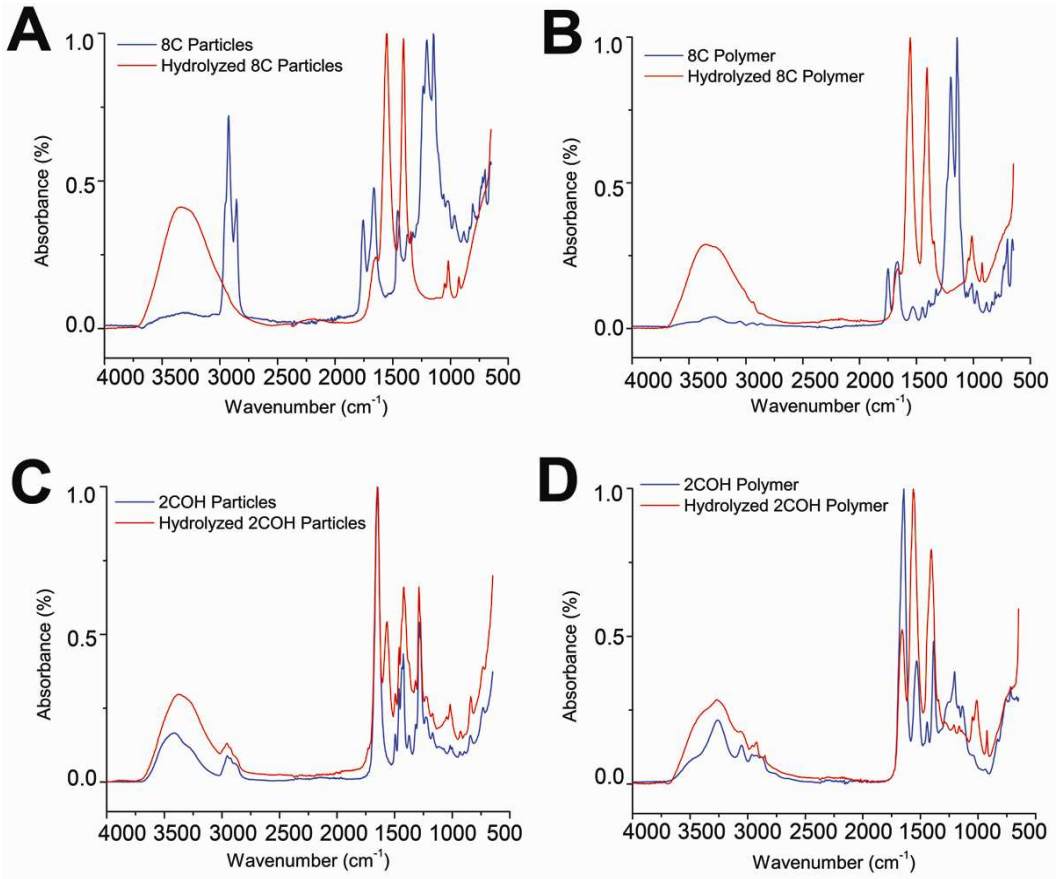

Figure 3.5: FTIR spectra of fluorinated nanoparticles. (A) Shows particles and (B) shows polymer prepared with 1H,1H-perfluoro-n-octyl acrylate monomer. (C) Shows particles and (D) shows polymer prepared with the 2-(allyl)hexafluoroisopropanol monomer. All solutions were allowed to evaporate prior to analysis of the resultant nanoparticle or polymer film.

Hydrolyzed particles showed a strong peak at 3326 cm^{-1}, which is within the hydrogen bonded OH region (3300 – 2500 cm^{-1}) and the primary aliphatic amine region (3450 – 3250 cm^{-1}). The emergence of the OH frequency was due to the hydrolysis of the perfluorinated acrylate (1H,H-perfluoro-n-octyl acrylate), which was hydrolyzed to a carboxylic acid.

Although the presence of an amine after hydrolysis suggests that the particles can be bound to a targeting ligand using simple chemistry, the fact that the fluorinated ester was hydrolyzed indicates that particles prepared with the 1H,H-perfluoro-n-octyl acrylate monomer would not be suitable for use as an active targeting agent if conversion to the primary amine is necessary. There was no evidence of ether hydrolysis.

The non-hydrolyzed particles prepared with the 1H,H-perfluoro-n-octyl acrylate showed a peak at 1753 cm^{-1} suggesting a carbonyl ester (1750 – 1725 cm^{-1}) and an amide I carbonyl peak (1670 – 1650 cm^{-1}), both of which were absent in the hydrolyzed particles' spectrum. The hydrolyzed particles also showed an N-H deformation peak at 1548 cm^{-1}, which is near the typical region (1650 – 1580 cm^{-1}) but was likely shifted to higher frequency due to hydrogen bonding. This would indicate the presence of an amine. Representative structures of the non-hydrolyzed and hydrolyzed particles are shown in Figure 3.6.

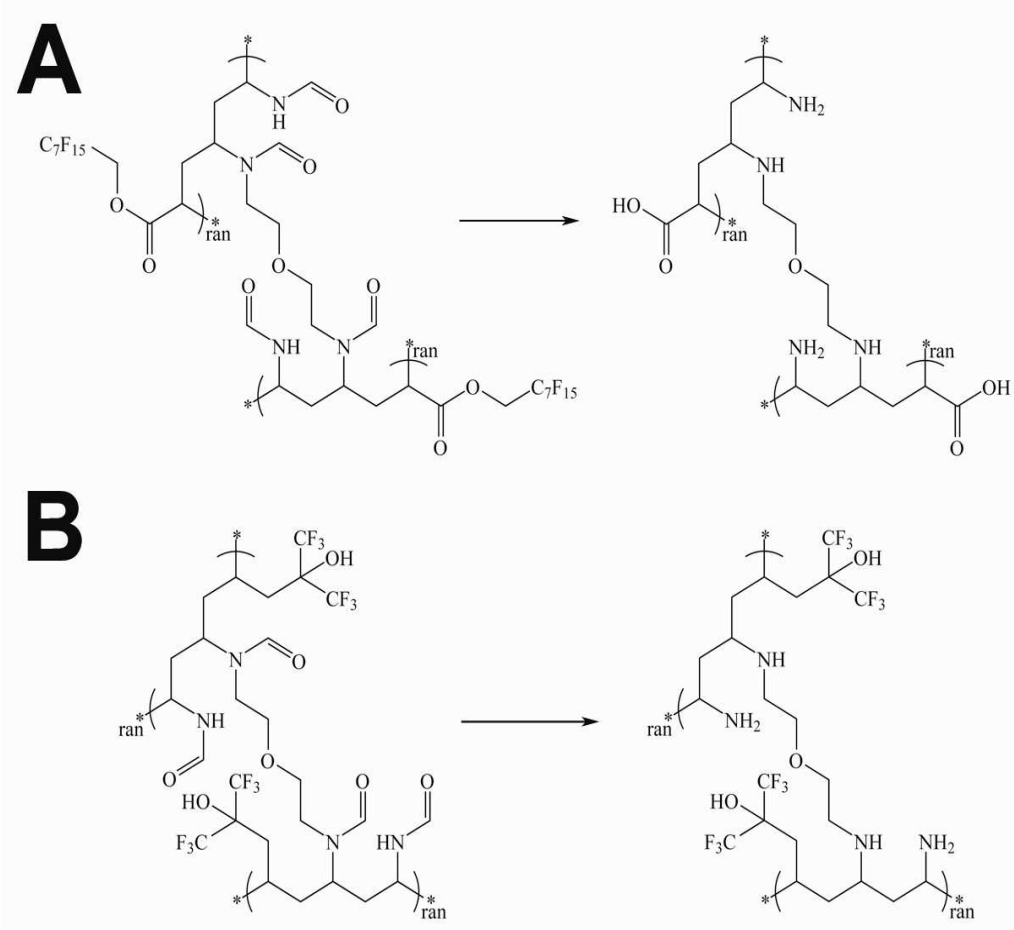

Figure 3.6: Representative chemical structures of non-hydrolyzed and hydrolyzed particles prepared using the different monomers. (A) Hydrolysis of particles prepared using the 1H,1H-perfluoro-n-octyl acrylate monomer, where amide groups were hydrolyzed to their corresponding amines, and the fluorinated ester was also cleaved. (B) Hydrolysis of particles prepared using the 2-(allyl)hexafluoroisopropanol monomer, where the amide groups were converted to primary and secondary amines, while the fluorinated regions remained intact.

The analogous polymer samples (Figure 3.5, Panel B) synthesized with the 1H,H-perfluoro-n-octyl acrylate monomer showed much evidence of hydrolysis. The hydrolyzed polymer spectrum showed a broad peak

around 3300 cm^{-1}, which is indicative of both OH stretching (3300 – 2500 cm^{-1}) and primary amines (3450 – 3250 cm^{-1}). The non-hydrolyzed spectrum showed small peaks at 1749 cm^{-1} and 1669 cm^{-1}, both of which were absent in the hydrolyzed spectrum and indicated the presence of a carbonyl ester (1750 – 1725 cm^{-1}) and an amide I (carbonyl) peak (1670 – 1650 cm^{-1}), respectively. Additionally, two peaks at 1196 cm^{-1} and 1140 cm^{-1} were present in the non-hydrolyzed spectrum, and indicated the presence of an ester C-O stretch. These peaks were very obviously absent in the hydrolyzed spectrum, which suggested the hydrolysis of the fluorinated ester group.

Nanoparticles prepared using the 2-(allyl)hexafluoroisopropanol monomer (Figure 3.5, Panel C) qualitatively suggested hydrolysis of the formamide group on the N-vinylformamide monomer and the (1,5-N-vinylformamido) ethyl ether crosslinker. The non-hydrolyzed spectrum showed a peak at 3401 cm^{-1}, which is within the OH stretch region (3300 – 2500 cm^{-1}). Unfortunately, this overlaped with the primary amine region (3450 – 3250 cm^{-1}), making it difficult to distinguish the two. The hydrolyzed particles showed a broad peak at 3378 cm^{-1}. Because this frequency is shifted toward the primary amine region and is at higher intensity, it stands to reason that this peak was due to influence from both the hydroxyl group on the 2-(allyl)hexafluoroisopropanol monomer and the

primary amine from the hydrolyzed formamide groups. Additionally, both spectra showed peaks at 1648 cm^{-1}, which suggested the presence of a hydrogen-bonded carbonyl group. This is most likely from the formamide group (amide I), which was present in the non-hydrolyzed particles and was likely present within the hydrolyzed particles to some degree, possibly buried within the particles where they might be sterically shielded from hydrolysis. The high intensity of this peak is not observed in the linear hydrolyzed polymer, which suggested that the crosslinking may have buried some of the formamide groups within the particles. The presence of an amine after hydrolysis suggested that these particles could be successfully conjugated with a carboxyl terminated targeting ligand. Representative structures of the hydrolyzed and non-hydrolyzed particles are shown in Figure 3.6. Like in the previous sample, there was no evidence of ether hydrolysis.

The spectra for the analogous polymer samples (Figure 3.5, Panel D) show evidence of formamide hydrolysis. Like the particles, both the hydrolyzed and non-hydrolyzed polymers show peaks in the OH stretch region (3300 – 2500 cm^{-1}), which is expected from to the 2-(allyl)hexafluoroisopropanol monomer. This region overlaps with the primary aliphatic amine region (3450 – 3250 cm^{-1}) and is more intense for the hydrolyzed polymer, suggesting that this peak is influenced by both

the hydroxyl group and the primary amine. Additional evidence for hydrolysis is the decrease in the intensity of the carbonyl peak (1650 cm^{-1}), which is likely shifted to a higher frequency in both spectra due to hydrogen bonding. The lower intensity of this peak in the hydrolyzed sample could indicate the loss of the formamide group, which would be expected. The fact that this peak did not diminish in intensity in the particles could be due to the crosslinking, which might bury formamide groups within the particles, again rendering them sterically isolated from hydrolysis.

^{19}F NMR Spectroscopy: Nanoparticle samples were analyzed using ^{19}F-NMR to determine their potential as ^{19}F-MRI contrast agents. Figure 3.7 shows the ^{19}F-NMR spectra of the fluorinated nanoparticles.

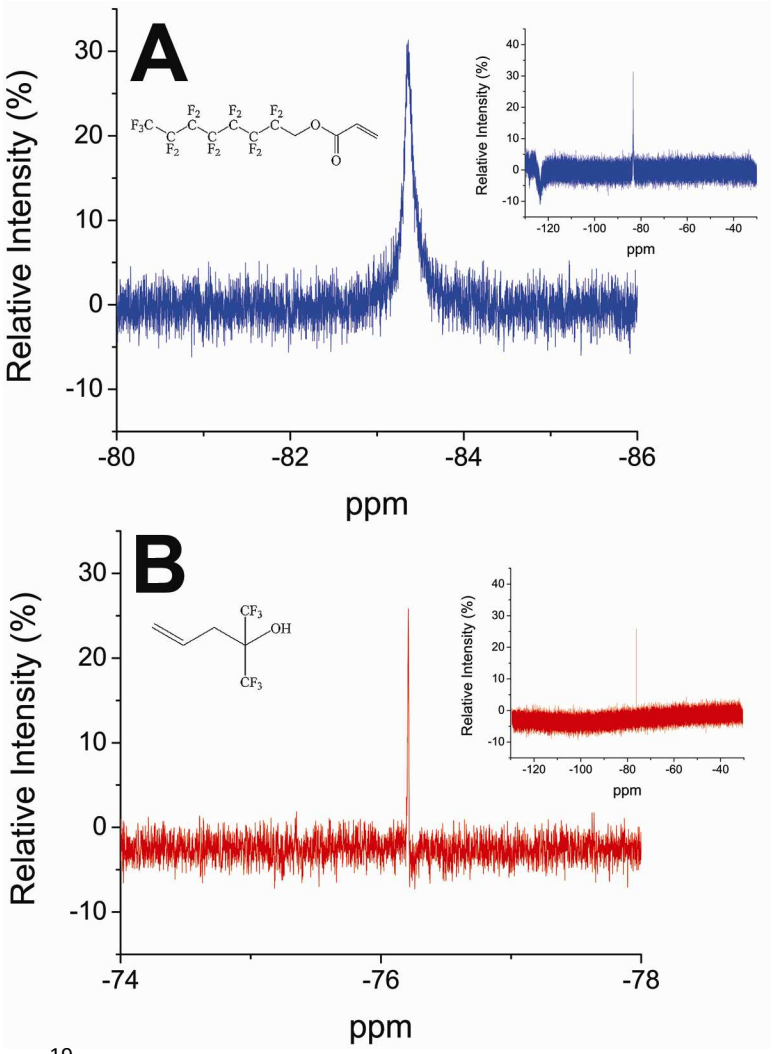

Figure 3.7: ^{19}F-NMR spectra of fluorinated nanoparticles. (A) The spectrum for nanoparticles prepared using the 1H,1H-perfluoro-n-octyl acrylate monomer, which showed a broad peak at -83.35 ppm. (B) The spectrum for nanoparticles prepared using the 2-(allyl)hexafluoroisopropanol monomer, which showed a sharp peak at -76.21 ppm. Insets show the spectra for the entire sweep width.

Particles prepared with the 1H,H-perfluoro-n-octyl acrylate monomer showed a peak between -83 ppm and -84 ppm (Figure 3.7, Panel A). This

peak is from the CF_2 group closest to the oxygen atom. Additionally, the spectrum shows an out-of-phase signal near -121 ppm (inset), which is from the perfluorinated region (-CF_2CF_2-) of the pendant group. Particles prepared with the 2-(allyl)hexafluoroisopropanol monomer show a peak around -76 ppm (Figure 3.7, Panel B). This peak is similar to the CF_2 peak from the 1H,H-perfluoro-n-octyl acrylate particles because both have the same proximity to a nearby oxygen atom. Both particles exhibit fairly narrow widths in their ^{19}F-NMR spectra, suggesting that some fluorinated groups are well solvated with a degree of mobility. This suggests that the particles would produce a signal in ^{19}F-MRI and would therefore be suitable for use as a ^{19}F-MRI contrast agent.[27]

3.4 Discussion

Current studies in the area of ^{19}F MRI contrast agents have validated the premise of developing colloidally stable, fluorinated contrast agents using nanoemulsions that contain a liquid perfluorocarbon phase. These studies have investigated fluorinated liquids such as perfluoro-15-crown-5-ether and perfluorooctyl bromide, which were emulsified into an aqueous phase using an appropriate biocompatible surfactant.[46, 47, 49, 51] Other studies have created novel fluorinated amphiphilic block copolymers that formed micelles in water, typically using a living free radical polymerization

method.[12, 27, 32, 33] In a previous study, the idea of synthesizing fluorinated nanoparticles using a single step, free radical polymerization technique was validated.[68] In this study, fluorinated nanoparticles were prepared using a free radical polymerization method that contained a hydrophilic monomer, a hydrophilic crosslinker, and one of two fluorinated monomers. Future studies will continue to optimize the reaction method to produce particles of smaller size by better controlling the reaction rate to encourage the formation of smaller molecular weight polymers, which could lead to smaller particles. After synthesis, the particles were evaluated for their suitability as a ^{19}F MRI contrast agent that can be targeted to specific pathological sites (e.g. tumors, atherosclerosis) using either active or passive targeting strategies.

A potential passive targeting strategy that has been investigated as a means to deliver antineoplastic agents to tumors exploits the anatomical and physiological abnormalities of tumor vasculature.[64] Typically, the blood vessels in tumor tissue are tortuous, poorly organized and contain numerous pores due to large gap junctions between endothelial cells, which can compromise lymphatic drainage.[63-67] These anatomical aberrations can cause extensive leakage of macromolecular agents and small nanoparticles from the capillaries into the tumor interstitium, where they can accumulate.[64] This phenomenon is called the enhanced

permeability and retention effect (EPR effect), and has been studied using macromolecular therapeutic agents.[73, 74] It has also been observed with polymeric nanoparticles that are several hundred nanometers in diameter.[75] Neutron scattering measurements and TEM images indicate that the particles prepared in this study are between approximately 200 nm and 400 nm in diameter, suggesting that they might be too large for passive targeting strategies.

Additionally, active targeting strategies using ligands that specifically bind selected tumor targets may amplify the specificity of nanoparticles.[62, 63] For example, amine-functionalized nanoparticles will react with ligands terminated with succinimide esters or isothiocyanates.[76] Carboxylated nanoparticles or ligands can be made reactive toward amine-terminated moieties using 1-ethyl-3-(dimethylaminopropyl)carbodiimide (EDC) and either N-hydroxysuccinimide (NHS) or N-hydroxysulfosuccinimide (sulfo-NHS) to form an amine-reactive succinimide ester.[76] FTIR spectra suggested that formamide groups on the surface of nanoparticles and linear polymers prepared in this study using the 2-(allyl)hexafluoroisopropanol fluorinated monomer can be hydrolyzed at high pH to liberate amine groups, yielding reactive sites for ligand conjugation to facilitate active targeting strategies.

Future studies will evaluate the reactivity of the amines and the amides to determine the most effective conjugation strategy for active targeting.

In addition to tumor imaging, another potential clinical application for nanoparticle-based MRI contrast agents is atherosclerosis imaging. This technique could prove useful in identifying patients at high-risk for myocardial infarction who have not been identified by routine clinical evaluation, and may also be useful in characterizing the vulnerability of atheroma present in high-risk areas of the coronary vasculature.[77] As an active targeting technique, nanoparticles could be conjugated with a ligand that would facilitate binding to proinflammatory adhesion molecules expressed during atherogenesis. Possible targets include intercellular cell-adhesion molecule-1 (ICAM-1) and vascular cell-adhesion molecule-1 (VCAM-1), both of which are overexpressed on the endothelium around atherosclerotic lesions.[77-79] Studies have also developed paramagnetic MRI contrast agents that actively target thrombus,[54, 80] and paramagnetic contrast agents have been designed to target integrins associated with angiogenesis because of the high vascularity of atherosclerotic lesions compared to normal vessel tissues.[81] Another study targeted macrophages, which are key effector inflammatory cells in atherosclerosis.[82] Analogous methods of targeting atheroma using ultrasound contrast agents have also been demonstrated.[79]

Although the linear polymers synthesized in this study were used only as a control, they could have diagnostic applications that should be evaluated in the future. For example, linear polymers synthesized from the 2-(allyl)hexafluoroisopropanol and N-vinylformamide monomers lacked visual turbidity in water, but presumably formed micelles approximately 200 nm in diameter, as estimated by dynamic light scattering measurements. The reactivity of the amide and amine groups (post hydrolysis) could facilitate conjugation with targeting ligands for active targeting strategies. Future studies will examine the possibility of using these fluorinated monomers as ^{19}F MRI contrast agents, and further examine the suitability of the crosslinked nanoparticles for use *in vivo*.

3.5 Conclusions

This work has aimed to further develop the use of fluorinated nanoparticles as ^{19}F MRI contrast agents. The results of this study suggested that fluorinated nanoparticles prepared using a simple free radical polymerization technique would produce a sufficient magnetic resonance signal for ^{19}F-MRI. Nanoparticles may be useful for passive targeting strategies that rely on phenomena such as the enhanced permeability and retention (EPR) effect, as well as active targeting strategies that rely on targeting ligands to amplify nanoparticle uptake into

pathological tissue, such as tumor tissue or atherosclerotic lesions. The results suggested that nanoparticles or polymers prepared using the 2-(allyl)hexafluoroisopropanol fluorinated monomer may be hydrolyzed to liberate free amines for possible conjugation with targeting ligands. Fluorinated imaging agents may ultimately prove to be safer and more effective than currently available paramagnetic contrast agents, such as gadolinium chelates, due to the demonstrated biocompatibility of fluorinated compounds. Future studies will examine the uptake of ligand-conjugated nanoparticles in *in vitro* cell culture, as well as the *in vivo* efficacy of fluorinated nanoparticles as ^{19}F-MRI contrast media.

Chapter 4

Fluorinated-Fluorescent Nanoparticles as *in vitro* Imaging Agents for Optical Fluorescence Imaging and Secondary Ion Mass Spectrometry (SIMS) Imaging

4.1 Introduction

Nanoparticles possess unique physical and chemical properties that make them useful for a variety of biomedical applications, including drug delivery and biomedical imaging. Several studies have utilized nanoparticles for a variety of *in vitro* and *in vivo* biomedical imaging techniques, including magnetic resonance imaging (MRI),[27, 31, 68] positron emission tomography (PET),[20] computed tomography (CT),[83] and optical fluorescence imaging.[84] In addition, nanoparticles can serve as a core platform for the integration of several functional moieties to facilitate synergistic imaging using multiple techniques.[85] For example, paramagnetic nanoparticles have been conjugated with radionuclides to facilitate integrated MRI and PET imaging, providing better spatial resolution and improved signal sensitivity.[86] Additionally, nanoparticles have been used to couple PET imaging with fluorescence imaging,[30] and paramagnetic nanoparticles have been integrated with fluorescent molecules to enable integrated MRI and optical fluorescence imaging.[87]

Mass spectrometry techniques, such as secondary ion mass spectrometry (SIMS) and matrix-assisted laser desorption/ionization (MALDI), are gaining recognition as high resolution *in vitro* biomedical imaging techniques.[15, 37, 44, 88] In SIMS imaging, a sample is bombarded with an electrostatically-focused primary ion beam, causing secondary

ions to be ejected from the surface, which are collected by a mass spectrometer (Figure 4.1).[16]

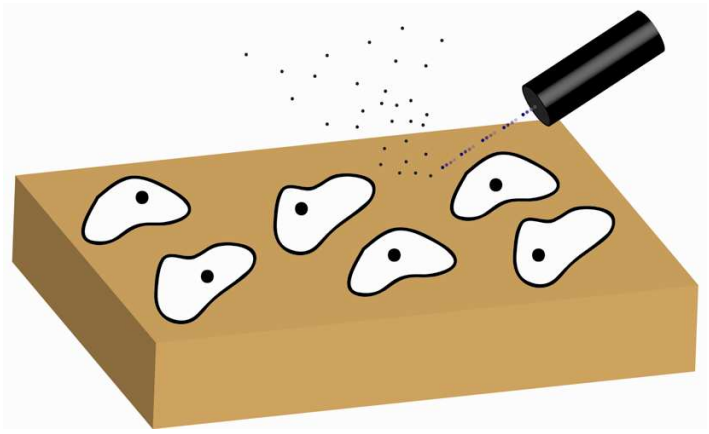

Figure 4.1: SIMS imaging of a cell sample. The sample is raster scanned by a primary ion beam, which causes secondary ions to be desorbed from the surface and collected by a mass spectrometer. The mass spectral data can then be compiled to generate a false-color image of the sample surface that is representative of the composition at each pixel.

As the primary ion beam is raster scanned across the surface of the sample, a mass spectrum can be obtained for each pixel, enabling the generation of images that are representative of the spatial distribution of specific ions desorbed from the sample surface.[13] SIMS has been used successfully for cellular and histological imaging,[88] and as a means to measure radiopharmaceutical distributions within cells.[89] SIMS imaging has also been used to measure natural isotopic ratios of carbon and nitrogen in cultured cells.[90] Additionally, SIMS has applications in the pharmacological evaluation of fluorinated drugs, like 5-fluorouracil, due to fluorine's biological rarity and high ion yield in SIMS.[88]

Multimodal imaging probes are quickly becoming important tools for advanced clinical diagnostics.[85] One way to mediate the specificity of an imaging probe to the site of interest is through active targeting mechanisms, such as conjugating an antibody or targeting ligand to the surface of the particle to facilitate binding to a cell surface antigen of interest. The LABL peptide (ITDGEATDSG) has been derived from leukocyte function associated antigen-1 (LFA-1) for this purpose. LFA-1 binds to intercellular adhesion molecule-1 (ICAM-1) on the surface of epithelial cells to facilitate leukocyte recruitment and extravasation to sites of inflammation.[78, 91] The LABL peptide has been shown to enhance nanoparticle uptake to ICAM-1 expressing cells when conjugated to the surface of drug-loaded nanoparticles.[72] By analogy, it should prove to be an effective means to target ICAM-1 expressing cells with multimodal nanoparticle imaging probes for *in vitro* imaging.

In this study, fluorinated-fluorescent nanoparticles were synthesized and evaluated as a potential multimodal *in vitro* imaging probe for optical fluorescence and SIMS imaging (Figure 4.2).

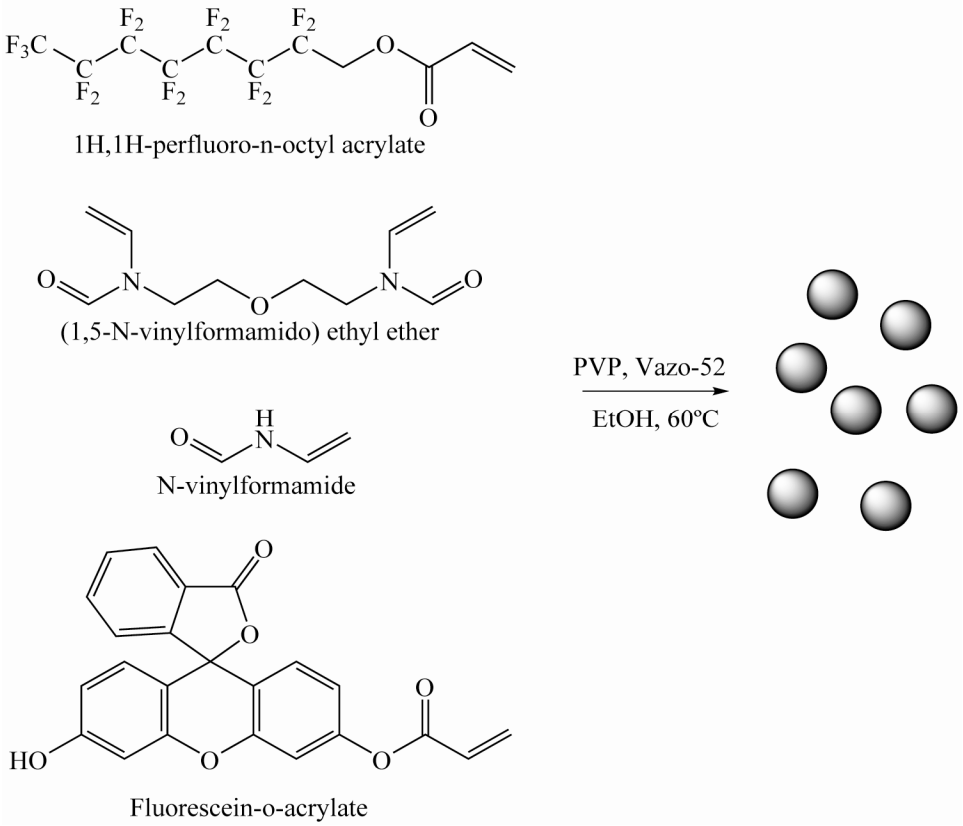

Figure 4.2: Synthesis of fluorinated-fluorescent nanoparticles. For each batch, monomers were dissolved in ethanol containing polyvinylpyrrolidone (PVP) as a surfactant and Vazo-52 initiator. The reaction was carried out at 60ºC for 24 hours.

Fluorine was selected as a SIMS imaging medium because of its biological rarity and high ion yield in SIMS.[16] Particles were conjugated with LABL peptide using an oxime formation strategy described previously that utilizes an aminooxy derivative of the LABL peptide to bind to formamide groups on the particles' surface (unpublished data) (Figure 4.3).

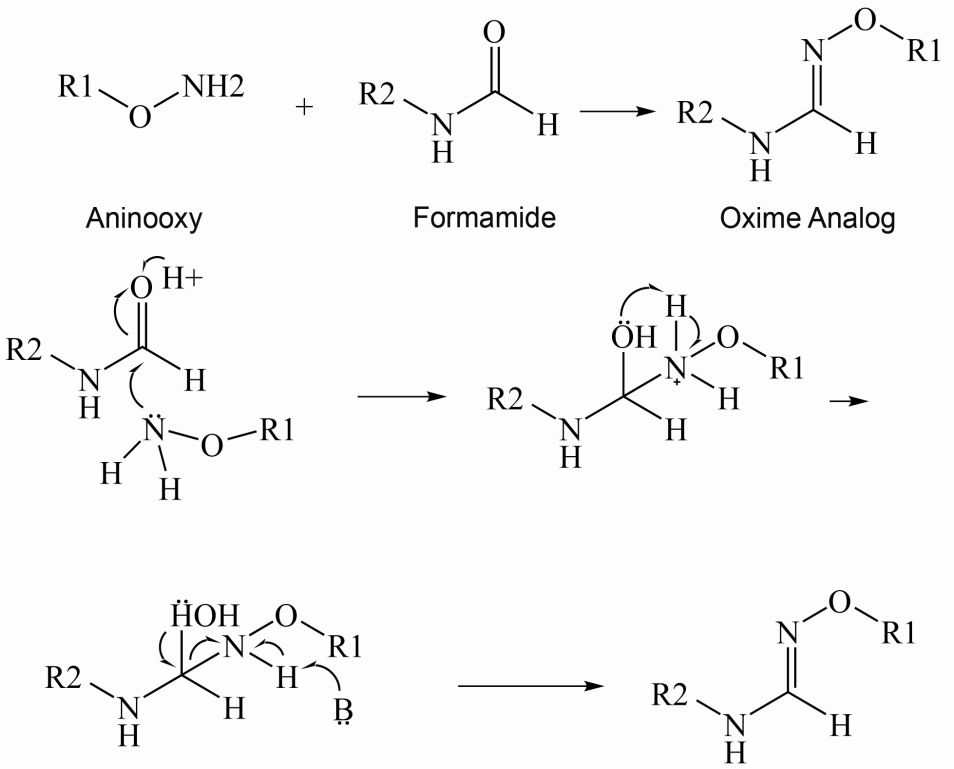

Figure 4.3: Proposed conjugation mechanism by oxime formation. The aminooxy group from the aminooxy-terminated LABL peptide attacks the carbonyl carbon of a formamide group on the surface of the particles. This induces the formation of a water leaving group, and the formation of an aldoxime-analog.

Other methods of using aminooxy derivatives to form oxime conjugates have been previously described.[92-94] Binding and internalization of conjugated nanoparticles in ICAM-1 expressing human umbilical cord vascular endothelial cells (HUVECs) was demonstrated using fluorescence imaging. The study suggests that these particles may be a useful probe for bimodal imaging using optical fluorescence and SIMS.

4.2 Materials and Methods

Materials: All materials were purchased from Sigma-Aldrich unless otherwise stated. 1H,H-perfluoro-n-octyl acrylate was purchased from ExFluor Research Corporation (Round Rock, TX). (E)-2,2'-(diazine-1,2-diyl)bis(2,4-dimethylpentanenitrile) (Vazo-52) was purchased from DuPont (Wilmington, DE). Dialysis membranes were purchased from Spectrum Labs (Rancho Dominquez, CA). Prior to nanoparticle synthesis, (1,5-N-vinylformamido) ethyl ether was synthesized as previously described.[59, 60] Impurities were precipitated out of N-vinylformamide using absolute ethanol and vacuum filtered prior to use. All other reagents were used as received.

Fluorinated-Fluorescent Nanoparticle Synthesis: Nanoparticles (NPs) were synthesized using a free radical polymerization method similar to one described previously.[68] First, 20 µL of 1H,H-perfluoro-n-octyl acrylate, 20 µL of (1,5-N-vinylformamido) ethyl ether and 20 µL of N-vinyl formamide were dissolved in absolute ethanol containing 0.015 g/mL polyvinylpyrrolidone (PVP) as a surfactant (MW approximately 360 kDa). Next, 0.0055 mg of fluorescein-o-acrylate and 0.0076 mg of Vazo-52 initiator were added to the solution under stirring. The reagent mixture was sparged with nitrogen for 10 minutes to remove dissolved oxygen,

then was heated in a silicone oil bath to 60℃ and stirred. The reaction was carried out isothermally under a nitrogen atmosphere for 24 hours. The reaction vessel was protected from ambient light to minimize photobleaching of the fluorescent monomer. The product was then dialyzed against deionized water using a 500 Da MWCO regenerated cellulose ester dialysis tube for 24 hours. The dialysate was changed at least 5 times to ensure complete solvent exchange and the removal of unreacted fluorescein-o-acrylate monomer. The resultant nanoparticle suspension was then purified by centrifugation for 1 hour at 18,000 rpm. Each centrifugation cycle was repeated at least 3 times. Particles were then flash-frozen in liquid nitrogen and lyophilized. After lyophilization, resuspended particle sizes and zeta potentials were measured using dynamic light scattering.

Aminooxylated LABL Peptide Synthesis: Aminooxy peptides were synthesized using 9-fluorenylmethyloxycarbonyl-protected amino acid chemistry on polyethylene glycol-polystyrene resins. The peptides synthesized where aminooxy LABL (aminooxy-ITDGEATDSG), an ICAM-1 antagonist. Peptides were deprotected, cleaved from resin, and isolated by precipitation in ether. Purification was completed using preparatory high performance liquid chromatography (HPLC), followed by

lyophilization. Peptide identity was verified and purity/content was assessed using analytical HPLC and mass spectroscopy.

Conjugation of Aminooxylated LABL Peptide to NPs: For the conjugation step, 5.9 mg of nanoparticles were re-suspended in 5.9 mL of 20 mM acetate buffer, to a final concentration of 1 mg/mL. Particles were then sonicated for 10 minutes to disperse the suspension. A volume of 3 mL (approximately 3 mg of nanoparticles) was transferred to a separate reaction flask, to which 21.43 mg of aminooxy-LABL (aminooxy-ITDGEATDSG) was added and dissolved by stirring. The pH of both the nanoparticle (NP) solution and LABL-conjugated NP solution (LABL-NPs) was measured and adjusted to pH 5.5. Reaction flasks were stirred at 500 RPM for 16 hours. Reaction time was based on previously conducted studies (unpublished data). After the reaction, the solution was extensively dialyzed against deionized H_2O (MWCO 3500 Da) to remove unreacted peptide, followed by lyophilization of the dialyzed product. Conjugation efficiency was measured using HPLC.

Up-regulation of ICAM-1 by Tumor Necrosis Factor-α: HUVECs (4.5×10^5 cells in 80 µl of serum free F12K medium) were stimulated using 1,000 U/ml of Tumor Necrosis Factor- α (TNF-α) for 24 hrs. Cells at the same

concentration were not activated and used as a control. HUVECs, with or without ICAM-1 upregulation, were incubated with 5% BSA in PBS for 10 min at 4 °C and then anti-ICAM-1-FITC (0.05 mg/ml) was added to cells and incubated at 4 ºC for 45 min. Free antibodies were removed by rinsing three times with PBS after centrifugation (4,000 RPM, 3 min). The fluorescence intensity of the cells was analyzed by flow cytometry. Data analysis was performed using Cell Quest software (BD).

Binding and Uptake of LABL-NPs by HUVECs: The binding and uptake of LABL-NPs was studied using fluorescence spectroscopy. TNF-α stimulated HUVECs (5 x 10^5 cells/ml) were added to a 96 well-plate (100 µl/well) and incubated with LABL-NPs or NPs (3.7 mg/ml, 30 µl) at 37 °C for 5, 15, 30 and 60 min and washed with PBS. The fluorescence intensity of cells was measured using a fluorescence plate reader (Spectramax M5; ex., 450 nm; em., 500 nm).

Fluorescence Microscopy of the Uptake of LABL-NPs by HUVECs: Fluorescence microscopy was used to compare the extent of binding and uptake of LABL-NPs and unconjugated NPs in HUVECs. HUVECs (2.5 x 10^5 cells/ml) were activated by using 1,000 U/ml TNF-α for 24 hrs. Cells were then added to an 8-well plate. LABL-NPs or unconjugated

fluorescent NPs (2.5 mg/ml) were incubated with the cells for 5, 15, 30 min and 1 hr at 37°C, 5% CO_2. Unbound nanoparticles were removed by washing three times with PBS and fixed with 4% paraformaldehyde. Nuclei were labeled with DAPI dilactate (blue) (300 nM, ex: 358 nm, em: 461 nm) for 5 min at 37ºC, 5% CO_2. Fluorescence micrographs were acquired using the UV and FITC filter sets of a Nikon Eclipse 80i microscope equipped for epifluorescence. Micrographs were captured using an Orca ER camera (Hamamatsu, Inc., Bridgewater, NJ) and analyzed by Metamorph, version 6.2 (Universal Imaging Corp., West Chester, PA).

Lysosomal Trafficking of LABL-NPs in HUVECs: Fluorescence microscopy was utilized to investigate the intracellular fate of LABL-NPs and untargeted NPs in HUVECs. HUVECs (2.5 x 10^5 cells/ml) were activated with 1,000 U/ml of TNF-α for 24 hrs. Cells were incubated with Texas red dextran (Mw 10,000, lysine fixable, 1 mg/ml) for 2 hours at 37°C, 5% CO_2 and washed three times with PBS. Cells were then incubated in serum free media at 37°C, 5% CO_2 for 12 hrs to allow the dye to reach the lysosomes. Afterward, LABL-NPs or unconjugated NPs (200 µl, 2.5 mg/ml) were added to cells and incubated for 5, 15, 30 and 60 min at 37°C, 5% CO_2. Unbound nanoparticles were removed by washing three

times with PBS. Nuclei were labeled with DAPI dilactate (blue) (300 nM, ex: 358 nm, em: 461 nm) for 5 min at 37ºC, 5% CO_2. Cells were then fixed with 4% paraformaldehyde. Fluorescence emissions of nanoparticles and lysosomes were observed using FITC and rhodamine filter sets, respectively (Nikon Eclipse 80i microscope equipped for epifluorescence). Micrographs were captured using an Orca ER camera (Hamamatsu, Inc.). Colocalization of nanoparticles with lysosomes was analyzed by Metamorph, version 6.2.

Development of Cell Sample Prep Method for SIMS Imaging: A cell sample preparation method was designed for SIMS imaging of nanoparticles in cells. A polished silicon disk was wiped clean several times with an ethanol-dampened, lint-free cloth. Residual dust was removed with pressurized nitrogen. The disk was placed into a 35-mm petri dish and covered with a fibronectin solution (25 ug/mL, Sigma) in PBS. After 3 hours at 4℃, the disk was removed, rinsed with PBS and placed in a 35-mm petri dish. A10 rat aorta smooth muscle cells (ATCC) maintained in DMEM containing 10% FBS at 37℃ in a 5% CO_2 incubator were seeded onto the disks at density of 1200 cells/cm^2. The disks were placed back into the incubator for 48 hours. The samples were then rinsed in PBS and fixed in 1% formaldehyde in PBS for 4 hours. The

samples were rinsed in PBS, then DI H_2O and were allowed to dry in the laminar hood for 4 hours.

TOF-SIMS (time of flight secondary ion mass spectrometry) was used to analyze the cell samples. TOF-SIMS experiments were performed on an Ion-TOF IV instrument equipped with both Bi (Bi_n^+, where n = 1 to 7) and SF_5^+ primary ion beam cluster sources. The analysis source was a pulsed, 25 keV bismuth cluster ion source (Bi_3^+), which bombarded the surface at an incident angle of 45 degrees to the surface normal. The target current was maintained at approximately 0.3 pA (± 10%) pulsed current with a raster size of 200 µm x 200 µm for all experiments. Both positive and negative secondary ions were extracted from the sample into a reflectron-type time of flight mass spectrometer. The secondary ions were then detected by a microchannel plate detector with a post-acceleration energy of 10 kV. A low energy electron flood gun was utilized for charge neutralization in the analysis mode. Each spectrum was averaged over a 60 s time period, with a cycle time of 100 µs. These conditions resulted in accumulated Bi_3^+ ion doses that were well below 10^{13} ions/cm^2.

Statistical Analysis: Statistical evaluation of data was performed using an analysis of variance (single-factor ANOVA). Tukey's test was used as a

post hoc analysis to assess the significance of differences. A value of $p < 0.05$ was accepted as significant.

4.3 Results and Discussion

Preparation of Fluorinated-fluorescent Nanoparticles: Fluorinated-fluorescent nanoparticles were prepared using a free radical polymerization method, similar to what has been described previously.[68] Nanoparticles were conjugated with aninooxy-LABL peptide using an oxime formation strategy, resulting in a conjugation efficiency of 93.8 % ± 0.05 % as measured by HPLC. Dynamic light scattering showed a mean particle diameter of 440 nm ± 4.3 nm for the unconjugated NPs and 354 nm ± 10 nm for the LABL-NPs (Table 4.1).

Table 4.1: Dynamic light scattering and zeta potential data for Nanoparticles

	Diameter (nm)	Polydispersity	Zeta Potential (mV)
NP	440 ± 4.3	0.21 ± 0.019	-5.08 ± 0.86
LABL-NP	354 ± 10	0.167 ± 0.083	-10.03 ± 3.27

The polydispersities for the particle samples were 0.21 ± 0.019 for the unconjugated NPs and 0.167 ± 0.083 for the LABL-NPs, and the measured zeta potentials were -5.08 mV ± 0.86 mV and -10.03 mV ± 3.27 mV for the unconjugated NPs and the LABL-NPs, respectively. The observed decrease in NP size after conjugation with the LABL peptide

could be due to increased colloidal stability arising after conjugation due to the increased surface charge magnitude, which results from the presence of anionic amino acid residues in the LABL peptide. Fluorinated groups on the NPs surface would be extremely hydrophobic, which might cause agglomeration, and hence an increased observed particle size for the unconjugated NPs. Presumably, these hydrophobic interactions are mitigated by the presence of the LABL peptide, which decreases the tendency of the NPs to agglomerate and hence the observed particle size.

Binding and uptake of nanoparticles in cells: Proinflammatory cytokines such as TNF-α have previously been shown to upregulate the expression if ICAM-1.[95] HUVECs were incubated with 1,000 U/ml of TNF-α for 24 hrs to induce overexpression of ICAM-1. HUVECs, with or without ICAM-1 upregulation, were incubated with anti-ICAM-1-FITC, which resulted in an approximately 32 x increase in ICAM-1 expression compared to HUVECs incubated in medium without TNF-α. The result confirmed the overexpression of ICAM-1 and validated the use of this cell line for this study (Figure 4.4).

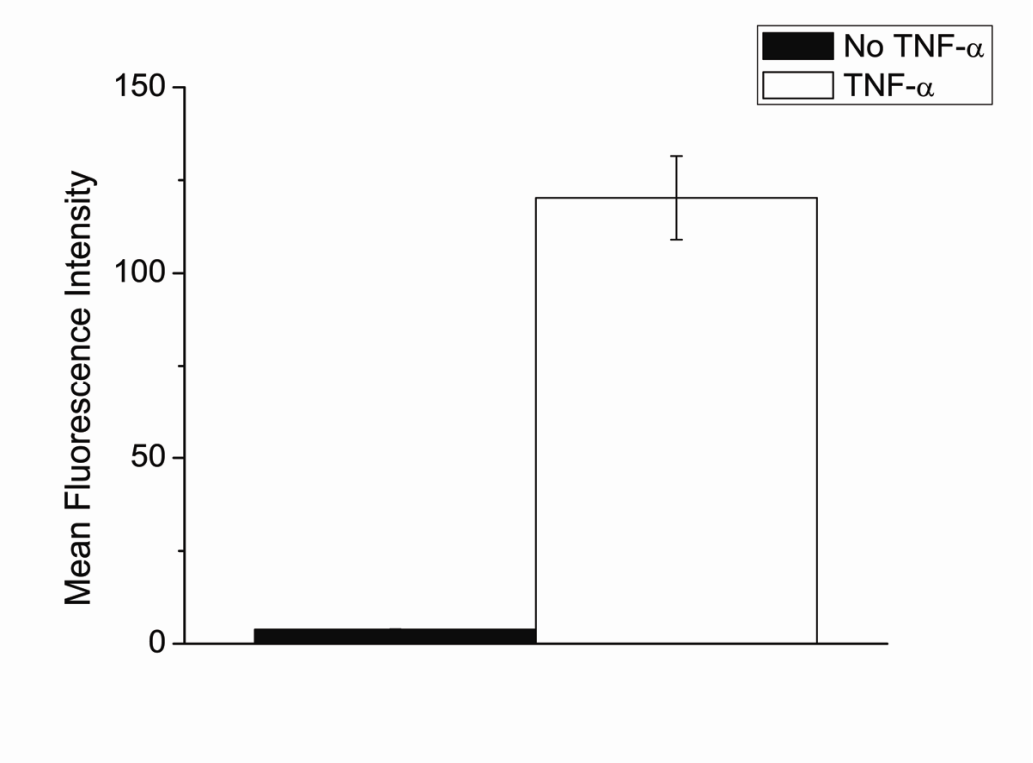

Figure 4.4: Upregulation of ICAM-1 expression in HUVECs incubated with TNF- α, as measured by the fluorescence intensity of anti-ICAM-1-FITC antibody. The results suggested an approximately 32 x increase in ICAM-1 expression after incubation with TNF- α. Error bars represent the standard deviation, with n=3.

Nanoparticles conjugated with LABL peptide were rapidly taken up by HUVECs, as determined by fluorescence measurements after incubation for several time points (Figure 4.5).

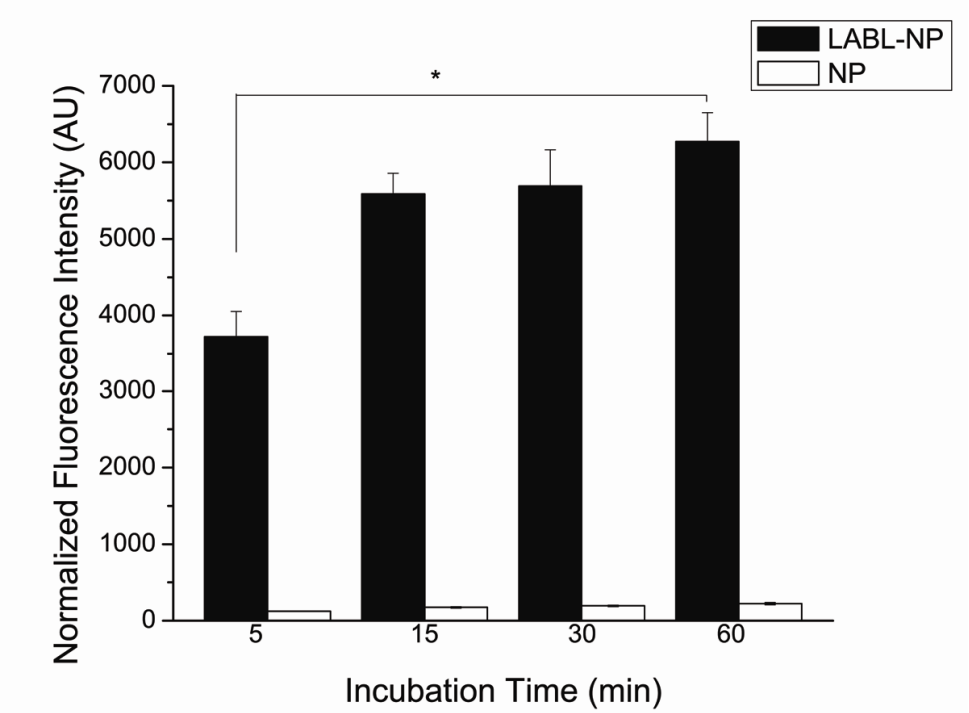

Figure 4.5: Normalized fluorescence intensity of LABL-conjugated NPs and non-conjugated NPs in HUVECs. The results suggested a much greater normalized fluorescence intensity for the LABL-conjugated nanoparticles, most likely due to binding facilitated by the LABL peptide. Data are presented by mean ± standard deviation. *$p<0.05$.

The normalized fluorescence intensity of the LABL-NPs was approximately 30 times greater after any incubation time (5 min to 60 min) than the normalized fluorescence intensity of the non-conjugated NPs, most likely due to binding to ICAM-1, which was facilitated by the LABL peptide. The enhanced binding of nanoparticles to ICAM-1 mediated through LABL and similar peptides has been described by others.[72, 96] Optical images showing fluorescence at several different time points

corroborate the quantitative fluorescence measurements (Figure 4.6), where nanoparticles (green) can be seen around cell nuclei (blue).

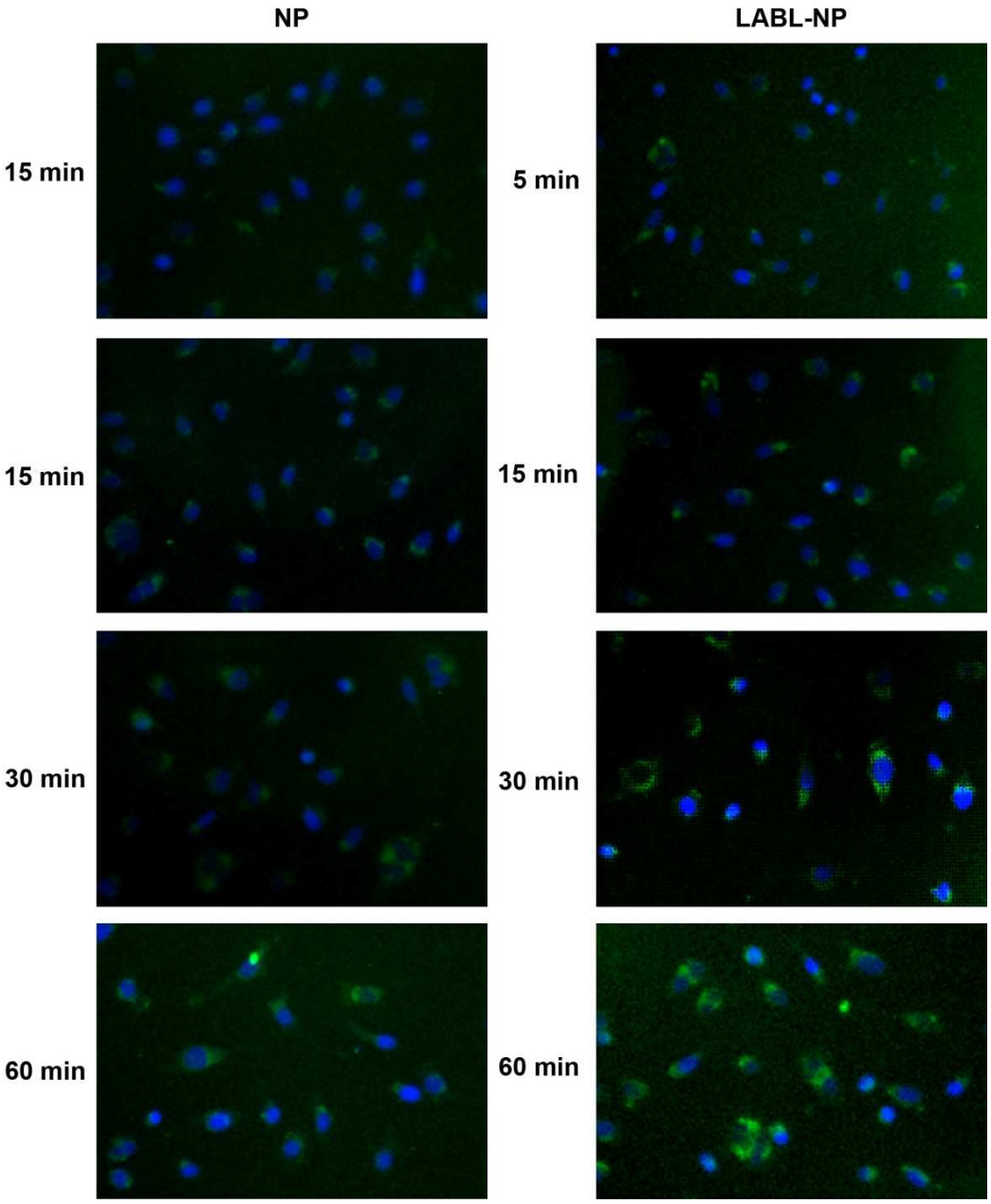

Figure 4.6: HUVECs after incubation with non-conjugated NPs and LABL-NPs. The results suggested that conjugation with the LABL peptide increases uptake of the particles into the cells.

Colocalization of NPs with lysosomes was analyzed using fluorescence imaging (Figure 4.7). Lysosomes are labeled red and NPs appear green. The results suggested that neither the LABL-conjugated NPs, nor the non-conjugated NPs, were trafficked to lysosomes, which would appear yellow in the image. This could be due to the large size of the nanoparticles (approximately 300 nm), which might be too large for endocytosis and/or lysosome trafficking. Alternatively, particles could be bound to the surface of cells. This result could be confirmed with SIMS analysis, which will analyze the surface of the cells and the internal composition of the cells by depth profiling.

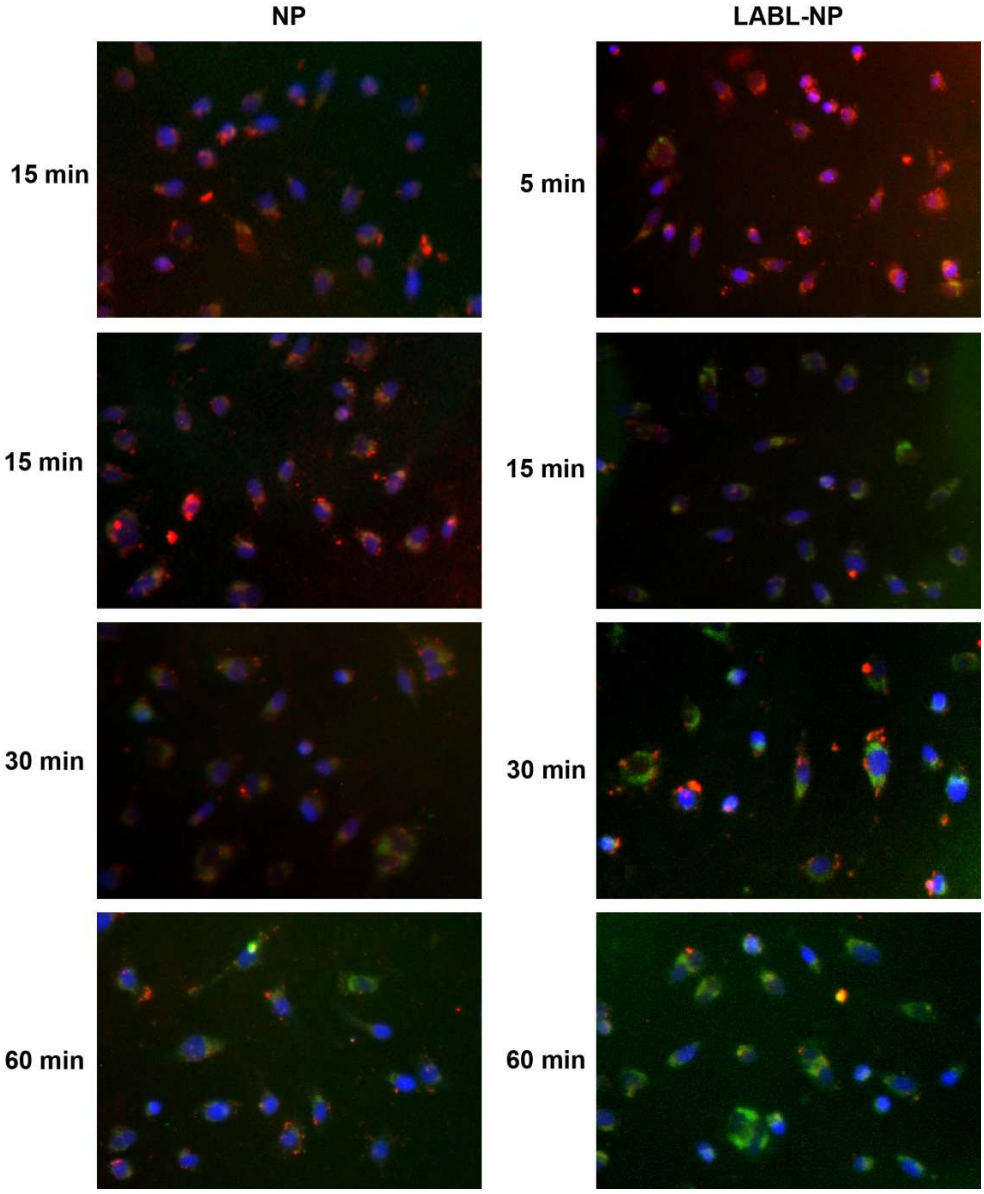

Figure 4.7: Colocalization of untargeted and targeted nanoparticles with lysosomes. Lysosomes were stained with Texas red dextran, and cell nuclei were stained with DAPI (blue). Colocalization of nanoparticles (green) with lysosomes would appear yellow. The results suggested that the nanoparticles were not incorporated within the lysosomes. This could be due to their large size (approximately 300 nm). We hypothesize that the particles were internalized via endocytosis, but were not incorporated into the lysosomes.

Cell Sample Preparation for SIMS Imaging: A sample preparation method for SIMS imaging of cells was developed using A10 rat aorta smooth muscle cells as a model cell line. Fixed A10 cells on silicon disks were imaged using a TOF-SIMS instrument equipped with an SF_5 sputter source and a Bi_3^+ analysis source. Cells were distinguishable before sputtering, but the surface contained many ions that would suggest the presence of residual salts, amino acids and proteins deposited from the growth medium and during substrate preparation (Figure 4.8). Images acquired after sputtering show less deposited material and greater contrast between the cells and the surrounding substrate. Amines, phosphates, and cholesterol are resolvable on the cell surfaces. The results suggest that this sample preparation method is suitable for producing high-resolution SIMS images of eukaryotic cells and may have applications in biomedical imaging. By incubating cells with an imaging probe that targets a specific cell surface antigen of interest; this technique could be used for *in vitro* diagnostic applications.

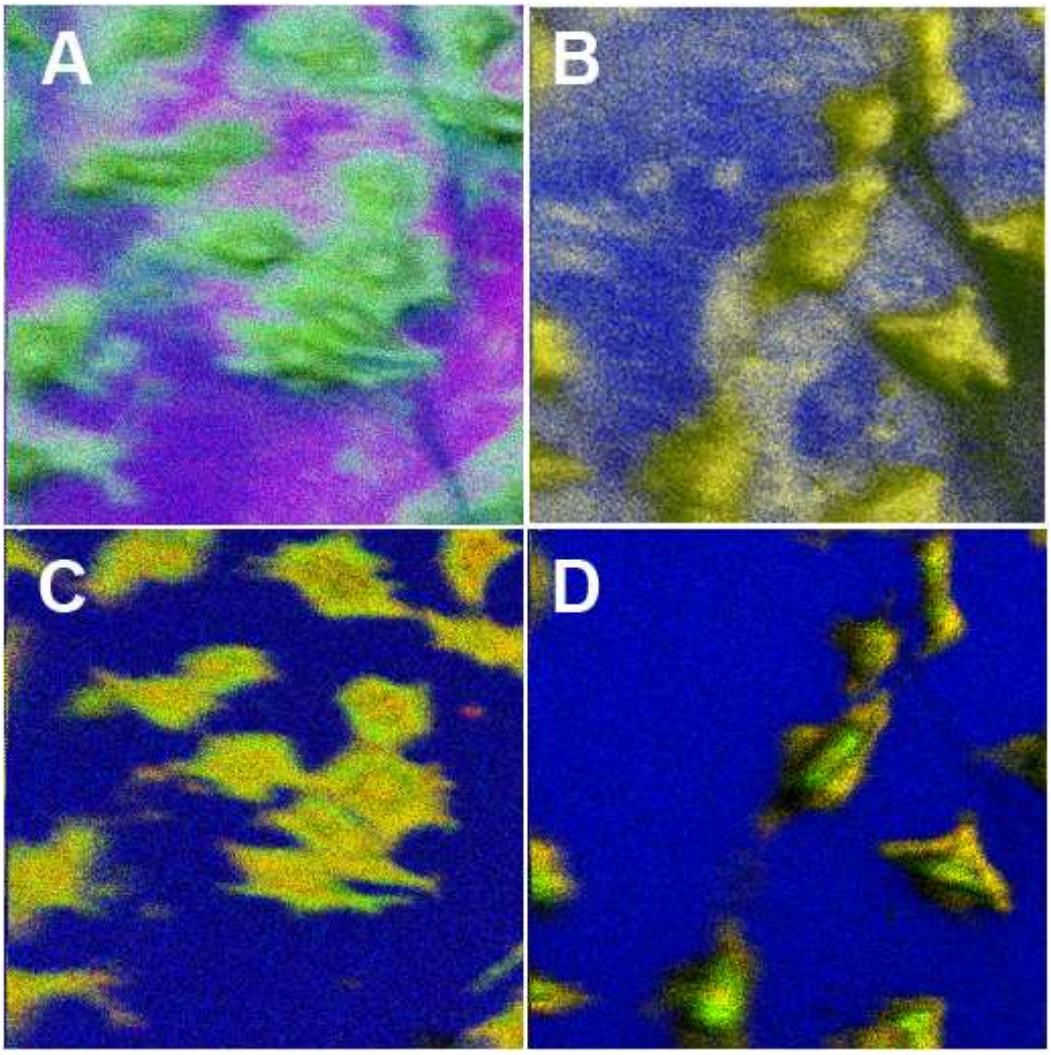

Figure 4.8: TOF-SIMS images of A10 rat aorta smooth muscle cells grown on a silicon substrate. Panels (A) and (B) were imaged before sputtering with SF_5, and (C) and (D) were imaged after sputtering. (A): Dark purple – amino acids; Light purple – sulfates; Green – phosphates. (B): Yellow – phospholipids; Blue – amino acids. (C): Yellow – amines and phosphates; Green – amines; Red – phosphates; Blue – silicon substrate. (D): Yellow – amino acids and phosphates; Green – cholesterol, amino acids and phosphates; Blue – silicon substrate.

4.4 Conclusions

Fluorinated-fluorescent nanoparticles with the potential for use as both an optical fluorescence imaging probe and a secondary ion mass spectrometry (SIMS) imaging probe have been described. Nanoparticles were conjugated with an ICAM-1 targeting ligand (LABL peptide) and showed enhanced binding to ICAM-1 expressing HUVECs when compared to non-conjugated particles. Nanoparticles were not shown to appreciably accumulate in lysosomes, possibly due to their large size. Additionally, a cell sample preparation method for SIMS imaging was developed using A10 rat aorta smooth muscle cells on a silicon substrate as a model. The images showed enhanced detail and less deposited material from the growth media after sputtering with SF_5, and areas containing amino acids, phosphates, phospholipids, and amines were easily distinguished from the silicon background. Present work is examining the suitability of fluorinated-fluorescent nanoparticles as SIMS imaging probes, which could be useful for diagnostic applications. Future work should examine the use of fluorinated-fluorescent nanoparticles as an optical fluorescent imaging probe and a SIMS imaging probe in samples of pathological interest.

Chapter 5

Conclusions and Future Directions

Fluorinated compounds have many applications in medicine, including oxygen transport, drug delivery vehicles, and contrast agents in medicine due to fluorine's unique chemical and nuclear properties. Fluorinated compounds have been used in microbubble contrast agents for ultrasound imaging, positron sources for PET imaging, and as an imaging probe in ^{19}F MRI. Additionally, fluorinated organic compounds generate a high ionization yield of fluorine in secondary ion mass spectrometry (SIMS), which is gaining recognition as an *in vitro* cellular imaging technique. This suggests that fluorinated SIMS "chromophores" could be developed for diagnostic imaging that target specific cell markers.

The goal of this work has been to develop a fluorinated nanoparticle platform technology that could be used for multiple biomedical imaging techniques, including *in vivo* and *in vitro* diagnostic imaging. Fluorinated nanoparticles were synthesized from one of two fluorinated monomers, as well as a hydrophilic monomer and hydrophilic crosslinker to enhance the aqueous colloidal stability of the nanoparticles. Nanoparticles were then characterized to determine their chemical properties, colloidal stability, and suitability for use as a ^{19}F MRI and SIMS contrast agent. Particle sizes were measured using small angle neutron scattering and dynamic light scattering, nuclear magnetic resonance signal was measured using ^{19}F NMR, and chemical functional groups

were determined using FTIR. Particle size and structure were also examined using scanning electron microscopy and transmission electron microscopy. The results suggested that nanoparticles are colloidally stable, exhibit a strong ^{19}F NMR signal and a high fluorinated ion yield in SIMS, and contain functional groups that would facilitate conjugation with antibodies or other ligands for targeted nanoparticle delivery to pathological tissues of interest for imaging.

Nanoparticles were also developed for bimodal optical fluorescence imaging and SIMS imaging by incorporating a fluorescent functionality within the particles. The fluorescent-fluorinated nanoparticles were conjugated with LABL peptide, which binds to ICAM-1 on the surface of endothelial cells to facilitate T-cell recruitment to sites of inflammation. *In vitro* cell uptake studies show enhanced binding and uptake of LABL-conjugated fluorescent-fluorinated nanoparticles compared to non-conjugated nanoparticles, suggesting that this technique could be used as a targeting mechanism for cellular imaging. A cell preparation method was also designed for SIMS imaging, which showed great cellular detail. Current work is examining the suitability of fluorinated-fluorescent nanoparticles as SIMS imaging probes for diagnostic imaging using the cell preparation method designed for this work.

Future work with this nanoparticle technology platform should further examine the potential use of fluorinated nanoparticles and MRI contrast agents. This would include phantom imaging of nanoparticle suspensions at different concentrations, followed by *in vivo* animal imaging. Furthermore, nanoparticles could be conjugated with targeting ligands to facilitate binding to pathological sites for imaging applications, such as tumors or atherosclerotic plaque. Additionally, linear fluorinated polymers, which were initially created as a control group, could be evaluated for their potential use in imaging applications. Future work in the area of SIMS imaging and optical fluorescence imaging should examine the use of ligand-conjugated nanoparticles to probe pathological samples of interest to evaluate the diagnostic utility of these particles for clinically-relevant imaging of biopsied tissues and cells.

Appendices

Appendix A

Nuclear Magnetic Resonance (NMR) and Magnetic Resonance Imaging (MRI)

Nuclear magnetic resonance is a phenomenon observed in atomic nuclei with net unpaired nuclear spins. Spin is a fundamental quantum mechanical property of all elementary particles. It is mathematically similar to angular momentum; however spin can only have discrete values in one of two spin states. Both of these states have the same energy, and hence are degenerate. Analogous to a spinning charged particle in classical physics, an elementary particle with a net spin and a charge also possesses a magnetic moment. The magnetic moment interacts with an external magnetic field, generating a torque on the particle.[10, 25]

$$W = \mu \times B_o$$

where W is the torque, μ is the magnetic moment vector, and B_o is the external magnetic field. In the absence of other effects, the torque would rotate the magnetic moment into alignment with the external magnetic field.[10, 25] The nucleus also possesses a net angular momentum due to spin, so this alignment does not occur immediately. Instead, the magnetic moment precesses around the external field axis at the Larmor frequency, as shown in Figure A.1.

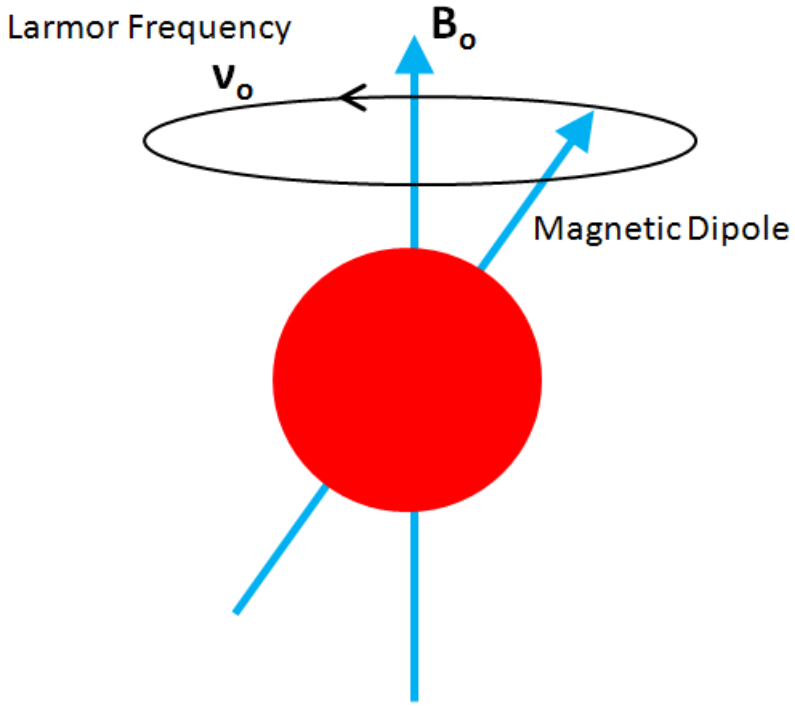

Figure A.1: Precession of a magnetic dipole in a magnetic field. The external magnetic field, B_o, exerts a torque on the magnetic moment (magnetic dipole) that would normally tend to make it align with the external magnetic field. However, the nucleus has angular momentum, so the magnetic moment precesses at the Larmor frequency (ν_o) around the external magnetic field (B_o).[10, 25]

$$\nu_o = \gamma \cdot B_o$$

where ν_o is the Larmor frequency, and γ is the gyromagnetic ratio of the nucleus. The gyromagnetic ratio is given by the following equation:

$$\gamma = \frac{\mu}{L} \propto \frac{q}{m}$$

where L is the angular momentum of the nucleus, q is the charge, and m is the mass of the nucleus.[10, 25] The value of the gyromagnetic ratio

increases with increasing nuclear charge (atomic number) and decreases with increasing mass (mass number). It is worth noting that atomic nuclei without unpaired nuclear spins (i.e. possess an even number of nucleons) do not possess a magnetic moment and hence do not exhibit nuclear magnetic resonance. Gyromagnetic ratio values of physiologically relevant atomic nuclei are listed in table A.1.[25]

Table A.1: Gyromagnetic ratios for atomic nuclei of physiological interest.

Nucleus	γ (MHz/T)
^{1}H	42.58
^{13}C	10.71
^{19}F	40.08
^{23}Na	11.27
^{31}P	17.25

Because of the two possible degenerate states of the nuclear spin, magnetic moments will align themselves with the external magnetic field in either a parallel or anti-parallel state. The anti-parallel state is slightly more energetic than the parallel state, thus slightly more nuclei will be in the parallel state than the anti-parallel state.[10] This generates a net magnetic moment (M_o) within the tissue that precesses at the Larmour frequency. The energy difference between the two spin states is given by:

$$\Delta E = \frac{-\gamma \hbar B_o}{2\pi}$$

where h is the Planck constant.[25] The ratio of parallel to anti-parallel spin states is given by:

$$\frac{n_+}{n_-} = e^{\frac{-\Delta E}{k_B T}}$$

where k_B is the Boltzmann constant and T is the temperature.[25] Because the energy difference between the two degenerate spin states is much smaller than the k_BT energy, this equation can be expanded to give an expression for M_o in the tissue:

$$M_o \approx \frac{n\mu^2 B_o}{k_B T}$$

where n is the total spin density ($n_+ + n_-$).[25] Thus, the equilibrium magnetization vector increases in magnitude as the strength of the external magnetic field increases. This sets the scale for the magnitude of the NMR signal, and is the primary motivation for doing MRI at high magnetic field strengths.

As described in Chapter 1, a typical MRI experiment consists of a transverse magnetic field that oscillates at the Larmor frequency of the nuclei of interest. This causes the magnetization vector to “flip” in the direction of the transverse field. If left alone, the flipped vector will decay back to its equilibrium position (M_o) in partial alignment with B_o.[25] This

phenomenon is called free induction decay (FID) and occurs as an exponential decay function dependent on the T2 relaxation time. As the amplitude of the transverse magnetic field is increased, the “flip angle” increases proportionately. Flip angle notation is often used in MRI, where a 90º pulse would mean a transverse magnetic field pulse with sufficient amplitude to “flip” the magnetization vector 90º.[25]

MRI pulse sequences incorporating several different flip angle magnetic pulses are often used during imaging to enhance the NMR signal. One common pulse sequence is the spin echo pulse sequence, which begins with a 90º pulse and finishes with a 180º pulse several precession periods later. An illustration of this sequence is shown in Figure A.2.

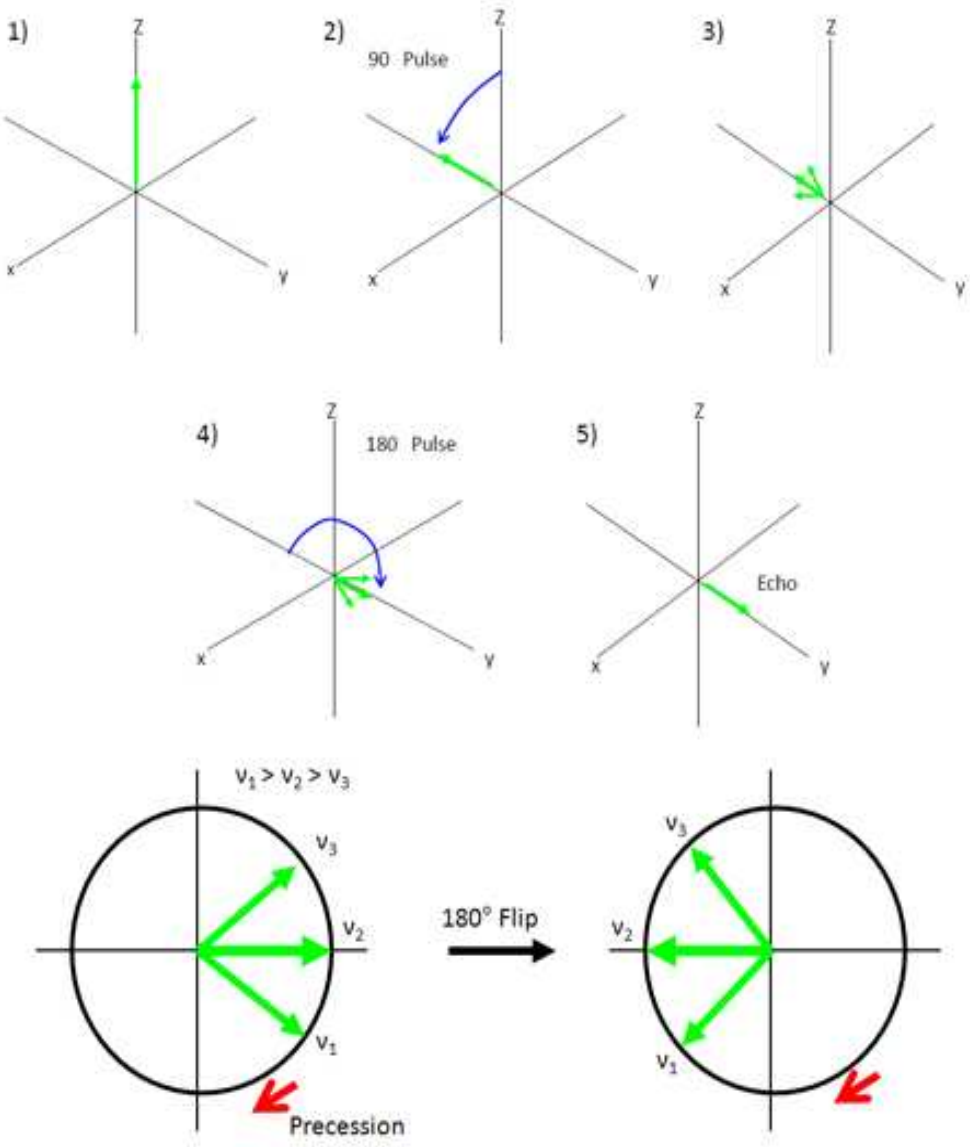

Figure A.2: Spin echo pulse sequence. A 90º pulse is applied to M_o (2), which is then allowed to precess for several periods. As this occurs, B_o inhomogeneities cause nuclei to precess at slightly different frequencies (3), thereby causing the magnetization vector to dephase. After a 180º pulse (4), the vector rephases as the component vectors acquire a negative phase. This produces a spin echo (5), overcoming the dephasing limitations of B_o field inhomogeneities.[25]

After the initial 90º pulse, the magnetization vector is allowed to precess for several periods. As the precession occurs, some nuclei begin to precess at different rates due to inhomogeneities in the B_o external field. This causes the magnetization vector to dephase into several vectors that precess at slightly different rates and have smaller magnitudes. By applying a 180º pulse, all vectors are converted to a negative phase angle, meaning that the vectors that were precessing at a faster rate are now behind the vectors precessing at a slower rate, causing the vectors to rephase as precession continues. This produces a spin echo, which can be measured by the MRI solenoid. This technique is the work horse of MRI because it can be used to overcome inhomogeneities in the B_o external field.[25]

The dynamics of the magnetization produced by nuclear magnetic dipoles in an external magnetic field have been modeled by the Swiss physicist Felix Bloch in 1946.[25] The Bloch equations include terms for precession, as well as exponential relaxation based on the T1 and T2 relaxation times. They are empirical equations designed to reproduce experimentally observed dynamics.

$$\frac{dM_x}{dt} = \gamma B_o M_y - \frac{M_x}{T_2}$$
$$\frac{dM_y}{dt} = -\gamma B_o M_x - \frac{M_y}{T_2}$$
$$\frac{dM_z}{dt} = -\frac{M_z - M_o}{T_1}$$

where M_x, M_y, and M_z are the three spatial components of the magnetization vector, and M_o is the equilibrium magnetization.[25] The preceding equations describe relaxation and precession when only the external magnetic field is acting on the nuclear magnetic dipole, and does not account for the transverse magnetic pulse. To include this phenomenon, one has to convert the equations to a rotating frame of reference so that the oscillating field appears to be constant.[25]

$$\frac{dM_x}{dt} = \omega_{rot} M_y - \frac{M_x}{T_2}$$
$$\frac{dM_y}{dt} = -\omega_{rot} M_x - \frac{M_y}{T_2} + \omega_T M_z$$
$$\frac{dM_z}{dt} = -\frac{M_z - M_o}{T_1} - \omega_T M_y$$

In this set of equations, ω_{rot} is the apparent precession rate in this rotating frame of reference, and ω_T is an equivalent to a precession frequency around the transverse magnetic field ($\omega_T = \gamma B_T$).[25]

Appendix B

Secondary Ion Mass Spectrometry (SIMS)

Secondary ion mass spectrometry (SIMS) is a surface analysis technique that is widely used to analyze the elemental composition of thin films.[16] Until recently, its use in biological samples has been limited by the complex nature of biological systems and by the imprecision of available SIMS technology. Current research in biological applications of SIMS suggests that this technique holds promise as a means to generate both qualitative and quantitative pharmacological and toxicological data from living systems.[14, 90, 97]

SIMS is a technique that depends on the sputtering of secondary ions from the surface of the sample of interest using a beam of highly charged particles, as shown in Figure B.1.[16]

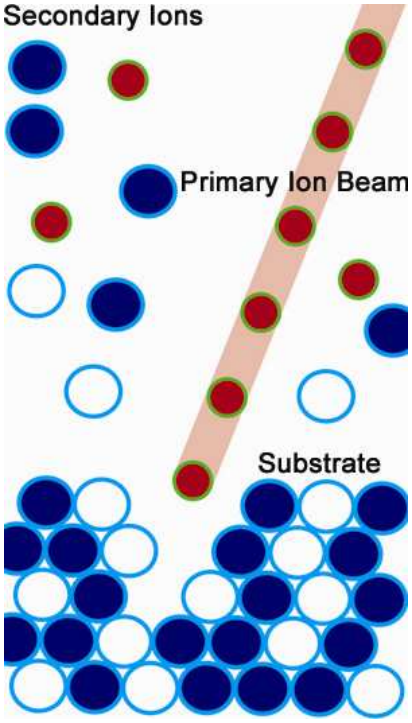

Figure B.1: Diagram of SIMS. The sample surface is bombarded with primary ions, causing material to be desorbed from the surface, some of which is ionized and collected by the mass spectrometer.

The impact from this primary ion beam causes secondary ions and polyatomic fragments to be ejected from the surface, where they are collected and analyzed by a mass spectrometer. Several different primary ion species are useful in SIMS, including Cs^+, O_2^+, O, Ar^+, and Ga^+ at energies between 1 keV and 30 keV.[16] The number of secondary ions produced as a function of sputtering is quantified by the sputter yield, which is the ratio of the number of atoms desorbed from the surface to the number of impinging primary ions. This value typically falls between 5 and 15 secondary ions per primary ion.[16] The secondary ion yield is the

fraction of desorbed material that becomes ionized and varies depending on the ionization potential of the species being ionized. Correlations between ionization potential and secondary ion yield are not exact and depend on the sample matrix and the sample itself.[16]

Sputtering effects can be described by the collision cascade model, where a high energy primary ion impacts a surface particle, transferring energy and momentum to an adjacent surface particle. This triggers a series of binary collisions, resulting in a change in the lattice structure of the sample and desorption of surface material.[13] Cluster ion sources can be used in SIMS to generate different sputtering effects. Typical monatomic primary ions (e.g. Cs^+, Ar^+, Ga^+) impact the surface at high energy, causing a large shift in the lattice structure, while only a small amount of material is desorbed from the surface. Conversely, a cluster ion primary beam (defined as any polyatomic ion species) has energy distributed to each atom in the cluster, thereby having a net effect of low energy primary ions impacting the surface of the sample. This produces less lattice disruption and causes more material to be ejected from the surface.[13]

As an example of cluster ion verses a monatomic ion as a sputter source, consider a 15 keV Ga^+ primary ion verses a 15 keV C_{60}^+ primary ion. The gallium ion will impact the surface with a kinetic energy of 15,000

eV, causing lattice disruption deep into the sample and minimal desorption of material.[13] In comparison, the 15,000 eV of the C_{60} ion will be distributed between 60 atoms, giving each carbon atom 250 eV of kinetic energy.[13] The C_{60} sputtering is localized to a depth of a few nanometers, causing minimal lattice disruption and a greater sputter yield. This is shown in Figure B.2.

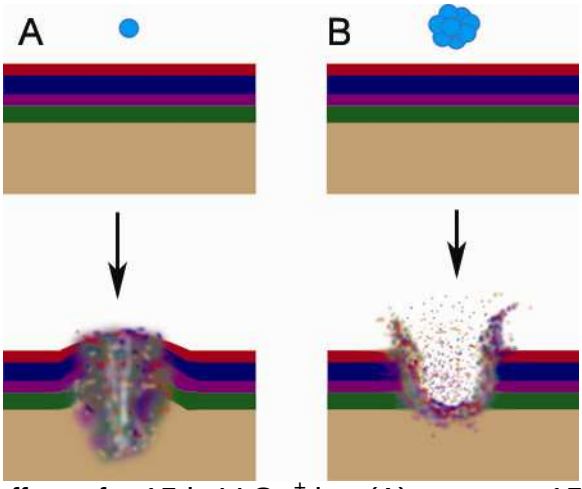

Figure B.2: The effect of a 15 keV Ga^+ ion (A) verses a 15 keV C_{60}^+ ion (B) in SIMS. The Ga^+ ion penetrates deeper into the substrate and at higher energy, causing lattice disruption and interlaminar mixing. The C_{60}^+ cluster ion has 250 eV per atom, which causes less lattice disruption and more material to be desorbed from the surface.[13]

In SIMS imaging, the primary ion beam raster scans the surface of the sample, collecting a mass spectrum for each pixel with a lateral resolution of about 100 nm.[13] The raw mass spectral data can be analyzed for specific ions of interest, which can be used to generate a two-dimensional compositional map of the sample surface (Figure B.3).

This technique can be used to generate images of biological samples showing the spatial distribution of compounds of interest, with a resolution of about 100 nm.[13] This is especially attractive for cell and tissue samples, which can be analyzed for specific biomarkers or targeting agents that have been introduced to enhance contrast.

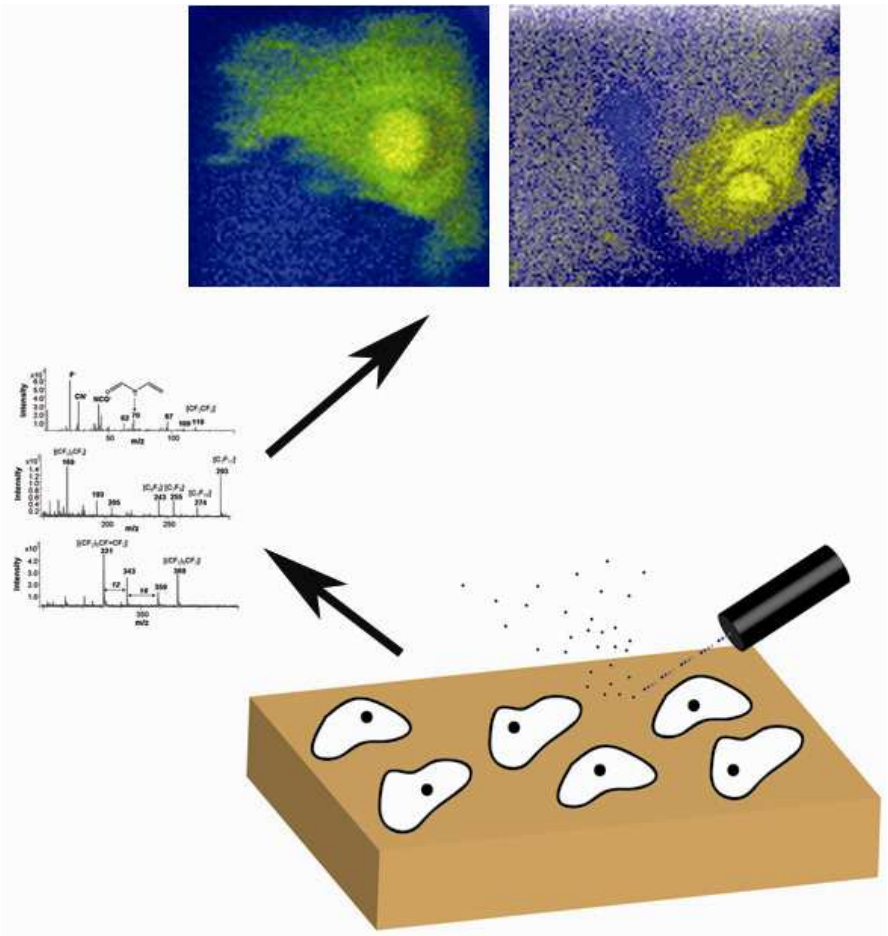

Figure B.3: Schematic of SIMS imaging. A cell sample is raster scanned in the SIMS instrument by the primary ion beam, which generates mass spectral data for each pixel. A two-dimensional composition map is generated from the raw data, which is effectively an image of the sample surface.

Appendix C

Small Angle Neutron Scattering (SANS)

Small angle neutron scattering (SANS) is a technique used to characterize structures in the nanometer size range and is ideally suited for studying polymers and colloids. Neutron scattering has several advantages over other scattering techniques such as X-ray scattering and light scattering. For instance, x-rays are scattered by the electrons surrounding a nucleus.[98] Consequently, heavy atoms (such as lead, mercury, etc.) scatter x-rays more efficiently than light atoms like carbon, oxygen and hydrogen. These lighter elements are the primary constituents of polymers, rendering them near invisible to x-rays. Neutron scattering is advantageous over light scattering because of a technique called contrast matching, in which isotopic differences in neutron scattering cross sections are exploited to enhance the contrast of the particles in the colloid with the background medium.[98] Additionally, in contrast to photons, neutrons interact with matter via nuclear forces rather than electrical forces, therefore they can penetrate deeper into matter.[98] The only disadvantage of neutron scattering is the relatively low neutron flux compared to other scattering techniques. Typical x-ray synchrotrons produce x-ray photons at a flux of 10^{18} photons per second per square

millimeter, while a typical neutron flux is on the order of 10^4 neutrons per second per square millimeter.[98]

Neutrons are generated for neutron scattering experiments with either nuclear reactors or spallation sources. Reactor neutrons are produced in a nuclear reactor by the fission of uranium fuel.[98] Spallation neutrons are produced using particle accelerators that bombard a heavy metal target with high-energy protons, causing neutrons to be ejected from the metal nuclei. Neutrons produced from these sources are "hot," with energies on the order of 10-100 MeV.[98] In order to be suitable for scattering experiments, neutrons must be made "cold." This is done by bringing them into thermal equilibrium with a moderating material that has a high scattering cross section, such as liquid hydrogen. This reduces the energy of the neutrons to about 5 MeV, which have a wavelength close to the typical interatomic distance and are therefore appropriate for scattering experiments.[98]

Neutron scattering occurs within a sample via elastic and inelastic scattering. In elastic scattering, there is no energy transfer between the incident neutron and the nucleus, thus only the direction of the neutron changes.[98, 99] With inelastic scattering, some of the kinetic energy is transferred to the nucleus, thus the magnitude of the neutron momentum vector changes in addition to its direction.[98, 99] This scattering depends on

the nuclear interaction potential between the neutron and the nucleus and decreases as the distance between them increases. This potential is very short range and decreases to zero at around 10^{-15} meters, which is much shorter than the wavelength of the cold neutrons (around 10^{-10} meters).[98] As a result, the nucleus acts as a point scatterer. An incident wave of neutrons has the wavefunction:[99]

$$\psi_i = e^{ikz}$$

where k is the incident neutron wave vector that points along the trajectory of the neutron and has magnitude $2\pi/\lambda$, where λ is the wavelength of the neutron. In this equation, z is the distance from the nucleus, and i is the imaginary unit. Because the nucleus acts as a point scatterer, the scattered wave will be spherically symmetrical with the wavefunction:[99]

$$\psi_s = \frac{-b}{r} e^{ik'r}$$

where b is the nuclear scattering length, r is the distance from the nucleus, and k' is the scattered neutron wave vector. The scattering length varies randomly across the periodic table, as well as between isotopes of the same element.[98, 99] This property is often exploited to enhance contrast between particles in a colloid and the surrounding medium. For example, hydrogen has a scattering length of -3.74×10^{-5} Å, and deuterium has a

scattering length of 6.67 x 10^{-5} Å.[100] By replacing an aqueous medium with deuterium oxide, the contrast between the colloidal particles and the aqueous medium can be enhanced. This technique is one of the key advantages of neutron scattering over other scattering techniques. A diagram of elastic neutron scattering is shown in Figure C.1.[98]

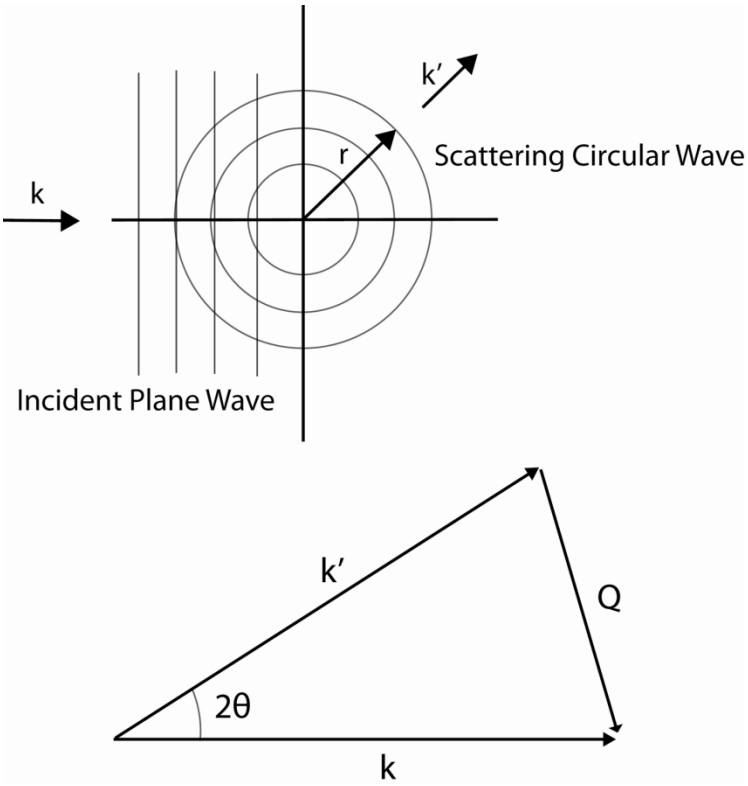

Figure C.1: Elastic neutron scattering from a fixed nucleus in space.

The incident and scattered wave vectors are given by k and k', respectively. The scattering vector is given by Q, which is the vector difference between k and k'.[98]

For an assembly of nuclei in space, the intensity of neutrons scattered at small angles is given by:[99]

$$I(Q) = \left| \int \rho(r) e^{iQ \cdot r} d^3 r \right|^2$$

Where ρ(r) is the scattering length density. In samples such as colloidal particles suspended in solution, the particles typically have a uniform scattering length density and are dispersed in a medium that also has a uniform scattering length density. In this case, the scattering intensity can be given by:[99]

$$I(Q) = (\rho_p - \rho_m)^2 N_p \left| \int_{V_p} e^{iQ \cdot r} d^3 r \right|^2$$

where ρ_p and ρ_m are the scattering length densities of the particles and the matrix, respectively. The number of particles is given by N_p, and the integral is taken over the entire volume, V_p. The integral term is called the form factor and is dependent on the geometry of the particles. For many simple shapes (e.g. spheres), the form factor can be easily obtained. For instance, the form factor for a sphere of radius r is given by:[99]

$$P(Q) = \left[\frac{3\left(\sin(Qr) - Qr \cdot \cos(Qr)\right)}{(Qr)^3} \right]^2$$

Other form factors exist for cylinders, ellipsoids, and more complicated geometries.

Raw SANS data are collected as intensity over polar space. For isotropic SANS experiments where intensity only changes as a function of radius from the origin in polar space, mathematical reduction techniques can be used to generate one-dimensional data sets of I(Q).[69] These data can be analyzed using a variety of model-independent techniques, as well as fit with various models that consider the geometry of the particles and the nature of their interactions. From these, one can derive information about particle size, polydispersity, molecular weight, and other particle properties.[69]

Bibliography

1. Riess, J. G., Fluorous micro- and nanophases with a biomedical perspective. *Tetrahedron* **2002,** 58, (20), 4113-4131.
2. Riess, J. G., Blood substitutes and other potential biomedical applications of fluorinated colloids. *Journal of Fluorine Chemistry* **2002,** 114, (2), 119-126.
3. Kirk, K. L., Fluorine in medicinal chemistry: Recent therapeutic applications of fluorinated small molecules. *Journal of Fluorine Chemistry* **2006,** 127, (8), 1013-1029.
4. Williams, D. E.; Houpt, D. J., Fluorine Nonbonded Potential Parameters Derived from Crystalline Perfluorocarbons. *Acta Crystallographica Section B-Structural Science* **1986,** 42, 286-295.
5. Bondi, A., Van Der Waals Volumes + Radii. *Journal of Physical Chemistry* **1964,** 68, (3), 441-&.
6. Barton, S. W.; Goudot, A.; Bouloussa, O.; Rondelez, F.; Lin, B. H.; Novak, F.; Acero, A.; Rice, S. A., Structural Transitions in a Monolayer of Fluorinated Amphiphile Molecules. *Journal of Chemical Physics* **1992,** 96, (2), 1343-1351.
7. Hsu, S. L.; Reynolds, N.; Bohan, S. P.; Strauss, H. L.; Snyder, R. G., Structure, Crystallization, and Infrared-Spectra of Amorphous Perfluoro-Normal-Alkane Films Prepared by Vapor Condensation. *Macromolecules* **1990,** 23, (21), 4565-4575.
8. Krafft, M. P.; Riess, J. G., Highly fluorinated amphiphiles and colloidal systems, and their applications in the biomedical field. A contribution. *Biochimie* **1998,** 80, (5-6), 489-514.
9. Riess, J. G.; Pace, S.; Zarif, L., Highly Effective Surfactants with Low Hemolytic-Activity. *Advanced Materials* **1991,** 3, (5), 249-251.
10. Allisy-Roberts, P.; Williams, J., *Farr's Physics for Medical Imaging*. Second ed.; Elsevier: New York, 2008.
11. Yu, J. X.; Kodibagkar, V. D.; Cui, W. N.; Mason, R. P., F-19: A versatile reporter for non-invasive physiology and pharmacology using magnetic resonance. *Current Medicinal Chemistry* **2005,** 12, (7), 819-848.
12. Matson, J. B.; Grubbs, R. H., Synthesis of fluorine-18 functionalized nanoparticles for, use as in vivo molecular imaging agents. *Journal of the American Chemical Society* **2008,** 130, (21), 6731-+.
13. Winograd, N., The magic of cluster SIMS. *Analytical Chemistry* **2005,** 77, (7), 142a-149a.

14. Guerquin-Kern, J. L.; Hillion, F.; Madelmont, J. C.; Labarre, P.; Papon, J.; Croisy, A., Ultra-structural cell distribution of the melanoma marker iodobenzamide: improved potentiality of SIMS imaging in life sciences. *Biomed Eng Online* **2004,** 3, 10.
15. Parry, S.; Winograd, N., High-Resolution TOF-SIMS Imaging of Eukaryotic Cells Preserved in a Trehelose Matrix. *Analytical Chemistry* **2005,** 77, (24), 7950-7957.
16. Benninghoven, A.; Rüdenauer, F. G.; Werner, H. W., *Secondary Ion Mass Spectrometry: Basic Concepts, Instrumental Aspects, Applications and Trends*. J. Wiley: New York, 1987.
17. Ametamey, S. M.; Honer, M.; Schubiger, P. A., Molecular imaging with PET. *Chemical Reviews* **2008,** 108, (5), 1501-1516.
18. Bars, D. L., Fluorine-18 and medical imaging: Radiopharmaceuticals for positron emission tomographystar, open. *Journal of Fluorine Chemistry* **2006,** 127, (11), 1488-1493.
19. Bangerter, M.; Kotzerke, J.; Griesshammer, M.; Elsner, K.; Reske, S. N.; Bergmann, L., Positron emission tomography with 18-fluorodeoxyglucose in the staging and follow-up of lymphoma in the chest. *Acta Oncologica* **1999,** 38, (6), 799-804.
20. Devaraj, N. K.; Keliher, E. J.; Thurber, G. M.; Nahrendorf, M.; Weissleder, R., F-18 Labeled Nanoparticles for in Vivo PET-CT Imaging. *Bioconjugate Chemistry* **2009,** 20, (2), 397-401.
21. Pisani, E.; Tsapis, N.; Galaz, B.; Santin, M.; Berti, R.; Taulier, N.; Kurtisovski, E.; Lucidarme, O.; Ourevitch, M.; Doan, B. T.; Beloeil, J. C.; Gillet, B.; Urbach, W.; Bridal, S. L.; Fattal, E., Perfluorooctyl Bromide Polymeric Capsules as Dual Contrast Agents for Ultrasonography and Magnetic Resonance Imaging. *Advanced Functional Materials* **2008,** 18, (19), 2963-2971.
22. Pisani, E.; Tsapis, N.; Paris, J.; Nicolas, V.; Cattel, L.; Fattal, E., Polymeric nano/microcapsules of liquid perfluorocarbons for ultrasonic imaging: physical characterization. *Langmuir* **2006,** 22, (9), 4397-402.
23. Zamorano, J. L.; Fernandez, M. A. G., *Contrast echocardiography in clinical practice*. 1 ed.; Springer: Milan, 2004.
24. Weller, G. E. R.; Villanueva, F. S.; Tom, E. M.; Wagner, W. R., Targeted ultrasound contrast agents: In vitro assessment of endothelial dysfunction and multi-targeting to ICAM-1 and sialyl Lewis. *Biotechnology and Bioengineering* **2005,** 92, (6), 780-788.
25. Buxton, R. B., *Introduction to Functional Magnetic Resonance Imaging: Principles and Techniques*. Cambridge University Press: New York, 2002.

26. Lauffer, R. B., Paramagnetic Metal-Complexes as Water Proton Relaxation Agents for Nmr Imaging - Theory and Design. *Chemical Reviews* **1987,** 87, (5), 901-927.
27. Du, W. J.; Nystrom, A. M.; Zhang, L.; Powell, K. T.; Li, Y. L.; Cheng, C.; Wickline, S. A.; Wooley, K. L., Amphiphilic Hyperbranched Fluoropolymers as Nanoscopic F-19 Magnetic Resonance Imaging Agent Assemblies. *Biomacromolecules* **2008,** 9, (10), 2826-2833.
28. Krafft, M. P., Fluorocarbons and fluorinated amphiphiles in drug delivery and biomedical research. *Advanced Drug Delivery Reviews* **2001,** 47, (2-3), 209-228.
29. Schwarz, R.; Schuurmans, M.; Seelig, J.; Kunnecke, B., F-19-MRI of perfluorononane as a novel contrast modality for gastrointestinal imaging. *Magnetic Resonance in Medicine* **1999,** 41, (1), 80-86.
30. Duconge, F.; Pons, T.; Pestourie, C.; Herin, L.; Theze, B.; Gombert, K.; Mahler, B.; Hinnen, F.; Kuhnast, B.; Dolle, F.; Dubertret, B.; Tavitian, B., Fluorine-18-labeled phospholipid quantum dot micelles for in vivo multimodal imaging from whole body to cellular scales. *Bioconjugate Chemistry* **2008,** 19, (9), 1921-1926.
31. Huang, M.; Huang, Z. L.; Bilgen, M.; Berkland, C., Magnetic resonance imaging of contrast-enhanced polyelectrolyte complexes. *Nanomedicine* **2008,** 4, (1), 30-40.
32. Janjic, J. M.; Srinivas, M.; Kadayakkara, D. K. K.; Ahrens, E. T., Self-delivering nanoemulsions for dual fluorine-19 MRI and fluorescence detection. *Journal of the American Chemical Society* **2008,** 130, (9), 2832-2841.
33. Peng, H.; Blakey, I.; Dargaville, B.; Rasoul, F.; Rose, S.; Whittaker, A. K., Synthesis and Evaluation of Partly Fluorinated Block Copolymers as MRI Imaging Agents. *Biomacromolecules* **2009,** 10, (2), 374-381.
34. Rieter, W. J.; Taylor, K. M. L.; An, H. Y.; Lin, W. L.; Lin, W. B., Nanoscale metal-organic frameworks as potential multimodal contrast enhancing agents. *Journal of the American Chemical Society* **2006,** 128, (28), 9024-9025.
35. Sharma, P.; Brown, S. C.; Bengtsson, N.; Zhang, Q. Z.; Walter, G. A.; Grobmyer, S. R.; Santra, S.; Jiang, H. B.; Scott, E. W.; Moudgil, B. M., Gold-Speckled Multimodal Nanoparticles for Noninvasive Bioimaging. *Chemistry of Materials* **2008,** 20, (19), 6087-6094.
36. Piehowski, P. D.; Carado, A. J.; Kurczy, M. E.; Ostrowski, S. G.; Heien, M. L.; Winograd, N.; Ewing, A. G., MS/MS Methodology To Improve Subcellular Mapping of Cholesterol Using TOF-SIMS. *Analytical Chemistry* **2008,** 80, (22), 8662-8667.

37. Altelaar, A. F. M.; van Minnen, J.; Jimenez, C. R.; Heeren, R. M. A.; Piersma, S. R., Direct molecular Imaging of Lymnaea stagnalis nervous tissue at subcellular spatial resolution by mass spectrometry. *Analytical Chemistry* **2005,** 77, (3), 735-741.
38. Baker, M. J.; Zheng, L.; Winograd, N.; Lockyer, N. P.; Vickerman, J. C., Mass Spectral Imaging of Glycophospholipids, Cholesterol, and Glycophorin A in Model Cell Membranes. *Langmuir* **2008,** 24, (20), 11803-11810.
39. Colliver, T. L.; Brummel, C. L.; Pacholski, M. L.; Swanek, F. D.; Ewing, A. G.; Winograd, N., Atomic and molecular imaging at the single-cell level with TOF-SIMS. *Analytical Chemistry* **1997,** 69, (13), 2225-2231.
40. Ostrowski, S. G.; Kurczy, M. E.; Roddy, T. P.; Winograd, N.; Ewing, A. G., Secondary ion MS imaging to relatively quantify cholesterol in the membranes of individual cells from differentially treated populations. *Analytical Chemistry* **2007,** 79, (10), 3554-3560.
41. Piehowski, P. D.; Kurczy, M. E.; Willingham, D.; Parry, S.; Heien, M. L.; Winograd, N.; Ewing, A. G., Freeze-etching and vapor matrix deposition for ToF-SIMS imaging of single cells. *Langmuir* **2008,** 24, (15), 7906-7911.
42. Roddy, T. P.; Cannon, D. M.; Ostrowski, S. G.; Winograd, N.; Ewing, A. G., Identification of cellular sections with imaging mass spectrometry following freeze fracture. *Analytical Chemistry* **2002,** 74, (16), 4020-4026.
43. Kulp, K. S.; Berman, E. S. F.; Knize, M. G.; Shattuck, D. L.; Nelson, E. J.; Wu, L. G.; Montgomery, J. L.; Felton, J. S.; Wu, K. J., Chemical and biological differentiation of three human breast cancer cell types using time-of-flight secondary ion mass spectrometry. *Analytical Chemistry* **2006,** 78, (11), 3651-3658.
44. Altelaar, A. F. M.; Klinkert, I.; Jalink, K.; de Lange, R. P. J.; Adan, R. A. H.; Heeren, R. M. A.; Piersma, S. R., Gold-enhanced biomolecular surface imaging of cells and tissue by SIMS and MALDI mass spectrometry. *Analytical Chemistry* **2006,** 78, (3), 734-742.
45. Kim, Y. P.; Oh, E.; Hong, M. Y.; Lee, D.; Han, M. K.; Shon, H. K.; Moon, D. W.; Kim, H. S.; Lee, T. G., Gold nanoparticle-enhanced secondary ion mass spectrometry imaging of peptides on self-assembled monolayers. *Analytical Chemistry* **2006,** 78, (6), 1913-1920.
46. Buchanan, G. W.; Moudrakovski, I., F-19 magnetic resonance imaging using vesicles of sucrose octaoleate-F-104. *Journal of Fluorine Chemistry* **2008,** 129, (2), 137-138.
47. Fan, X. B.; River, J. N.; Muresan, A. S.; Popescu, C.; Zamora, M.; Culp, R. M.; Karczmar, G. S., MRI of perfluorocarbon emulsion kinetics in

rodent mammary tumours. *Physics in Medicine and Biology* **2006,** 51, (2), 211-220.
48. Srinivas, M.; Morel, P. A.; Ernst, L. A.; Laidlaw, D. H.; Ahrens, E. T., Fluorine-19 MRI for visualization and quantification of cell migration in a diabetes model. *Magn Reson Med* **2007,** 58, (4), 725-34.
49. Flogel, U.; Ding, Z.; Hardung, H.; Jander, S.; Reichmann, G.; Jacoby, C.; Schubert, R.; Schrader, J., In vivo monitoring of inflammation after cardiac and cerebral ischemia by fluorine magnetic resonance imaging. *Circulation* **2008,** 118, (2), 140-8.
50. Neubauer, A. M.; Caruthers, S. D.; Hockett, F. D.; Cyrus, T.; Robertson, J. D.; Allen, J. S.; Williams, T. D.; Fuhrhop, R. W.; Lanza, G. M.; Wickline, S. A., Fluorine cardiovascular magnetic resonance angiography in vivo at 1.5 T with perfluorocarbon nanoparticle contrast agents. *J Cardiovasc Magn Reson* **2007,** 9, (3), 565-73.
51. Partlow, K. C.; Chen, J.; Brant, J. A.; Neubauer, A. M.; Meyerrose, T. E.; Creer, M. H.; Nolta, J. A.; Caruthers, S. D.; Lanza, G. M.; Wickline, S. A., 19F magnetic resonance imaging for stem/progenitor cell tracking with multiple unique perfluorocarbon nanobeacons. *Faseb J* **2007,** 21, (8), 1647-54.
52. Brigger, I.; Dubernet, C.; Couvreur, P., Nanoparticles in cancer therapy and diagnosis. *Advanced Drug Delivery Reviews* **2002,** 54, (5), 631-651.
53. Maeda, H.; Wu, J.; Sawa, T.; Matsumura, Y.; Hori, K., Tumor vascular permeability and the EPR effect in macromolecular therapeutics: a review. *Journal of Controlled Release* **2000,** 65, (1-2), 271-284.
54. Yu, X.; Song, S. K.; Chen, J.; Scott, M. J.; Fuhrhop, R. J.; Hall, C. S.; Gaffney, P. J.; Wickline, S. A.; Lanza, G. M., High-resolution MRI characterization of human thrombus using a novel fibrin-targeted paramagnetic nanoparticle contrast agent. *Magn Reson Med* **2000,** 44, (6), 867-72.
55. Shi, L. J.; Berkland, C., pH-Triggered dispersion of nanoparticle clusters. *Advanced Materials* **2006,** 18, (17), 2315-+.
56. Mahoney, C. M.; Fahey, A. J., Three-dimensional compositional analysis of drug eluting stent coatings using cluster secondary ion mass spectrometry. *Analytical Chemistry* **2008,** 80, (3), 624-632.
57. Mahoney, C. M.; Patwardhan, D. V.; McDermott, M. K., Characterization of drug-eluting stent (DES) materials with cluster secondary ion mass spectrometry (SIMS). *Applied Surface Science* **2006,** 252, (19), 6554-6557.

58. Mahoney, C. M.; Roberson, S. V.; Gillen, G., Depth profiling of 4-acetamindophenol-doped poly(lactic acid) films using cluster secondary ion mass spectrometry. *Analytical Chemistry* **2004,** 76, (11), 3199-3207.
59. Shi, L. J.; Berkland, C., Acid-labile polyvinylamine micro- and nanogel capsules. *Macromolecules* **2007,** 40, (13), 4635-4643.
60. Shi, L. J.; Khondee, S.; Linz, T. H.; Berkland, C., Poly(N-vinylformamide) nanogels capable of pH-sensitive protein release. *Macromolecules* **2008,** 41, (17), 6546-6554.
61. Caravan, P.; Ellison, J. J.; McMurry, T. J.; Lauffer, R. B., Gadolinium(III) chelates as MRI contrast agents: Structure, dynamics, and applications. *Chemical Reviews* **1999,** 99, (9), 2293-2352.
62. Brannon-Peppas, L.; Blanchette, J. O., Nanoparticle and targeted systems for cancer therapy. *Advanced Drug Delivery Reviews* **2004,** 56, (11), 1649-1659.
63. Cho, K. J.; Wang, X.; Nie, S. M.; Chen, Z.; Shin, D. M., Therapeutic nanoparticles for drug delivery in cancer. *Clinical Cancer Research* **2008,** 14, (5), 1310-1316.
64. Iyer, A. K.; Khaled, G.; Fang, J.; Maeda, H., Exploiting the enhanced permeability and retention effect for tumor targeting. *Drug Discovery Today* **2006,** 11, (17-18), 812-818.
65. Matsumura, Y.; Maeda, H., A New Concept for Macromolecular Therapeutics in Cancer-Chemotherapy - Mechanism of Tumoritropic Accumulation of Proteins and the Antitumor Agent Smancs. *Cancer Research* **1986,** 46, (12), 6387-6392.
66. Skinner, S. A.; Tutton, P. J. M.; Obrien, P. E., Microvascular Architecture of Experimental Colon Tumors in the Rat. *Cancer Research* **1990,** 50, (8), 2411-2417.
67. Suzuki, M.; Hori, K.; Abe, I.; Saito, S.; Sato, H., A New Approach to Cancer-Chemotherapy - Selective Enhancement of Tumor Blood-Flow with Angiotensin-Ii. *Journal of the National Cancer Institute* **1981,** 67, (3), 663-669.
68. Bailey, M. M.; Mahoney, C. M.; Dempah, K. E.; Davis, J. M.; Becker, M. L.; Khondee, S.; Munson, E. J.; Berkland, C., Fluorinated Copolymer Nanoparticles for Multimodal Imaging Applications. *Macromolecular Rapid Communications* **2010,** 31, (1), 87-92.
69. Kline, S. R., Reduction and analysis of SANS and USANS data using IGOR Pro. *Journal of Applied Crystallography* **2006,** 39, 895-900.
70. Munter, A. Scattering Length Density Calculator. http://www.ncnr.nist.gov/resources/sldcalc.html (1 November),
71. Sears, V. F., Neutron Scattering Lengths and Cross Sections. *Neutron News* **1992,** 3, (3), 29-37.

72. Chittasupho, C.; Xie, S. X.; Baoum, A.; Yakovleva, T.; Siahaan, T. J.; Berkland, C. J., ICAM-1 targeting of doxorubicin-loaded PLGA nanoparticles to lung epithelial cells. *Eur J Pharm Sci* **2009,** 37, (2), 141-50.
73. Nakanishi, T.; Fukushima, S.; Okamoto, K.; Suzuki, M.; Matsumura, Y.; Yokoyama, M.; Okano, T.; Sakurai, Y.; Kataoka, K., Development of the polymer micelle carrier system for doxorubicin. *Journal of Controlled Release* **2001,** 74, (1-3), 295-302.
74. Satchi-Fainaro, R.; Puder, M.; Davies, J. W.; Tran, H. T.; Sampson, D. A.; Greene, A. K.; Corfas, G.; Folkman, J., Targeting angiogenesis with a conjugate of HPMA copolymer and TNP-470. *Nature Medicine* **2004,** 10, (3), 255-261.
75. Kim, J. H.; Kim, Y. S.; Park, K.; Lee, S.; Nam, H. Y.; Min, K. H.; Jo, H. G.; Park, J. H.; Choi, K.; Jeong, S. Y.; Park, R. W.; Kim, I. S.; Kim, K.; Kwon, I. C., Antitumor efficacy of cisplatin-loaded glycol chitosan nanoparticles in tumor-bearing mice. *Journal of Controlled Release* **2008,** 127, (1), 41-49.
76. McCarthy, J. R.; Weissleder, R., Multifunctional magnetic nanoparticles for targeted imaging and therapy. *Advanced Drug Delivery Reviews* **2008,** 60, (11), 1241-1251.
77. Jaffer, F. A.; Libby, P.; Weissleder, R., Molecular and cellular imaging of atherosclerosis: emerging applications. *J Am Coll Cardiol* **2006,** 47, (7), 1328-38.
78. Anderson, M. E.; Siahaan, T. J., Mechanism of binding and internalization of ICAM-1-derived cyclic peptides by LFA-1 on the surface of T cells: a potential method for targeted drug delivery. *Pharm Res* **2003,** 20, (10), 1523-32.
79. Hamilton, A. J.; Huang, S. L.; Warnick, D.; Rabbat, M.; Kane, B.; Nagaraj, A.; Klegerman, M.; McPherson, D. D., Intravascular ultrasound molecular Imaging of atheroma components in vivo. *Journal of the American College of Cardiology* **2004,** 43, (3), 453-460.
80. Flacke, S.; Fischer, S.; Scott, M. J.; Fuhrhop, R. J.; Allen, J. S.; McLean, M.; Winter, P.; Sicard, G. A.; Gaffney, P. J.; Wickline, S. A.; Lanza, G. M., Novel MRI contrast agent for molecular imaging of fibrin: implications for detecting vulnerable plaques. *Circulation* **2001,** 104, (11), 1280-5.
81. Winter, P. M.; Morawski, A. M.; Caruthers, S. D.; Fuhrhop, R. W.; Zhang, H.; Williams, T. A.; Allen, J. S.; Lacy, E. K.; Robertson, J. D.; Lanza, G. M.; Wickline, S. A., Molecular imaging of angiogenesis in early-stage atherosclerosis with alpha(v)beta3-integrin-targeted nanoparticles. *Circulation* **2003,** 108, (18), 2270-4.

82. Jaffer, F. A.; Libby, P.; Weissleder, R., Molecular Imaging of cardiovascular disease. *Circulation* **2007,** 116, (9), 1052-1061.
83. El-Gendy, N.; Aillon, K. L.; Berkland, C., Dry powdered aerosols of diatrizoic acid nanoparticle agglomerates as a lung contrast agent. *Int J Pharm* **2010,** 391, (1-2), 305-12.
84. Gao, J. H.; Chen, K.; Xie, R. G.; Xie, J.; Yan, Y. J.; Cheng, Z.; Peng, X. G.; Chen, X. Y., In Vivo Tumor-Targeted Fluorescence Imaging Using Near-Infrared Non-Cadmium Quantum Dots. *Bioconjugate Chemistry* **2010,** 21, (4), 604-609.
85. Cheon, J.; Lee, J. H., Synergistically integrated nanoparticles as multimodal probes for nanobiotechnology. *Acc Chem Res* **2008,** 41, (12), 1630-40.
86. Choi, J. S.; Park, J. C.; Nah, H.; Woo, S.; Oh, J.; Kim, K. M.; Cheon, G. J.; Chang, Y.; Yoo, J.; Cheon, J., A hybrid nanoparticle probe for dual-modality positron emission tomography and magnetic resonance imaging. *Angewandte Chemie-International Edition* **2008,** 47, (33), 6259-6262.
87. Kircher, M. F.; Mahmood, U.; King, R. S.; Weissleder, R.; Josephson, L., A multimodal nanoparticle for preoperative magnetic resonance imaging and intraoperative optical brain tumor delineation. *Cancer Research* **2003,** 63, (23), 8122-8125.
88. Fragu, P.; Kahn, E., Secondary ion mass spectrometry (SIMS) microscopy: A new tool for pharmacological studies in humans. *Microscopy Research and Technique* **1997,** 36, (4), 296-300.
89. Chehade, F.; de Labriolle-Vaylet, C.; Moins, N.; Moreau, M. F.; Papon, J.; Labarre, P.; Galle, P.; Veyre, A.; Hindie, E., Secondary ion mass spectrometry as a tool for investigating radiopharmaceutical distribution at the cellular level: The example of I-BZA and C-14-I-BZA. *Journal of Nuclear Medicine* **2005,** 46, (10), 1701-1706.
90. Peteranderl, R.; Lechene, C., Measure of carbon and nitrogen stable isotope ratios in cultured cells. *Journal of the American Society for Mass Spectrometry* **2004,** 15, (4), 478-485.
91. Yusuf-Makagiansar, H.; Yakovleva, T. V.; Tejo, B. A.; Jones, K.; Hu, Y. B.; Verkhivker, G. M.; Audus, K. L.; Siahaan, T. J., Sequence recognition of alpha-LFA-1-derived peptides by ICAM-1 cell receptors: Inhibitors of T-cell adhesion. *Chemical Biology & Drug Design* **2007,** 70, (3), 237-246.
92. Gajewiak, J.; Cai, S. S.; Shu, X. Z.; Prestwich, G. D., Aminooxy pluronics: Synthesis and preparation of glycosaminoglycan adducts. *Biomacromolecules* **2006,** 7, (6), 1781-1789.

93. Hecker, J. G.; Berger, G. O.; Scarfo, K. A.; Zou, S. M.; Nantz, M. H., A flexible method for the conjugation of aminooxy ligands to preformed complexes of nucleic acids and lipids. *Chemmedchem* **2008,** 3, (9), 1356-1361.
94. Hwang, J. Y.; Li, R. C.; Maynard, H. D., Well-defined polymers with activated ester and protected aldehyde side chains for bio-functionalization. *Journal of Controlled Release* **2007,** 122, (3), 279-286.
95. Konno, S.; Grindle, K. A.; Lee, W. M.; Schroth, M. K.; Mosser, A. G.; Brockman-Schneider, R. A.; Busse, W. W.; Gern, J. E., Interferon-gamma enhances rhinovirus-induced RANTES secretion by airway epithelial cells. *American Journal of Respiratory Cell and Molecular Biology* **2002,** 26, (5), 594-601.
96. Zhang, N.; Chittasupho, C.; Duangrat, C.; Siahaan, T. J.; Berkland, C., PLGA nanoparticle--peptide conjugate effectively targets intercellular cell-adhesion molecule-1. *Bioconjug Chem* **2008,** 19, (1), 145-52.
97. Lechene, C.; Hillion, F.; McMahon, G.; Benson, D.; Kleinfeld, A. M.; Kampf, J. P.; Distel, D.; Luyten, Y.; Bonventre, J.; Hentschel, D.; Park, K. M.; Ito, S.; Martin; Schwartz; Benichou, G.; Slodzian, G., High-resolution quantitative imaging of mammalian and bacterial cells using stable isotope mass spectrometry. *Journal of Biology* **2006,** 5, (20), 20.1-20.30.
98. Pynn, R., Neutron Scattering - A Primer. *Los Alamos Science* 1990, pp 1-19.
99. Jackson, A. J., Introduction to Small-Angle Neutron Scattering. In National Institute of Standards and Technology (NIST), US Department of Commerce: Gaithersburg, MD, 2008; pp 1-24.
100. Rennie, A. R., Neutron Scattering from Polymers. In *Polymer Spectroscopy*, Fawcett, A. H., Ed. John Wiley & Sons, Ltd.: Chichester, England, 1996; pp 325-345.